



© Copyright by Nicholas A. Boggs 2014

All Rights Reserved

# A Cylindrical Dielectric Surface-Wave Antenna

A Thesis

Presented to

The Faculty of the Department of Electrical and Computer Engineering

University of Houston

In Partial Fulfillment

of the Requirements for the Degree

Master of Science

in Electrical Engineering

by

Nicholas A. Boggs

May 2014

# A Cylindrical Dielectric Surface-Wave Antenna

---

Nicholas A. Boggs

Approved:

---

Chair of the Committee  
Stuart A. Long, Professor,  
Electrical and Computer Engineering

Committee Members:

---

David R. Jackson, Professor,  
Electrical and Computer Engineering

---

Lowell Wood, Professor, Physics

---

Suresh K. Khator, Associate Dean,  
Cullen College of Engineering

---

Badrinath Roysam, Professor and Chair,  
Electrical and Computer Engineering

## **Acknowledgements**

I would like to thank my thesis advisor Dr. Stuart Long for always supporting me and guiding me throughout my time at University of Houston. Switching over from an aerospace engineering background to a master's in electrical engineering was exceedingly challenging. However, his enthusiasm for electromagnetics, motivation, constant leadership, and caring nature for people made it truly a pleasure to work with him. I am incredibly thankful that he gave me multiple opportunities to succeed. I would also like to thank Dr. David Jackson for shaping the problem in my master's thesis. His technical background, imagination and analytical capabilities fueled this thesis. His constant drive pushed this research analysis much further than I would have anticipated. I would not be graduating in such a short period of time without his efforts. I appreciate all hours that he spent working with me late in the evenings towards an analytical solutions, analysis and applications. To my lab partners Sohini Sengupta, Krishna Kota, and Anthony Lau you are all an amazing support group both intellectually and inspirationally. I will miss those brainstorming sessions and coffee runs. Lastly, I would like to thank my family for their endless support for constantly advising and motivating me towards my goals. I will miss those summer breaks staying in Virginia with them. And I am grateful that my father planted the seed back in 2010 for me to go back and obtain a master's degree. I had no intention of ever doing so at the time but eventually over the course of two years the seed produced roots.

# A Cylindrical Dielectric Surface-Wave Antenna

An Abstract

of a

Thesis

Presented to

the Faculty of the Department of Electrical and Computer Engineering

University of Houston

In Partial Fulfillment

of the Requirements for the Degree

Master of Science

in Electrical Engineering

by

Nicholas A. Boggs

May 2014

## **Abstract**

A new type of dielectric surface-wave antenna (DSWA) has been proposed using a tapered cylindrical dielectric structure. The structure is radially tapered in permittivity to produce a directive endfire beam that is omnidirectional in the azimuth direction. Unlike a dielectric resonator antenna (DRA) that uses a cavity mode to achieve radiation, this antenna uses a radially-propagating surface wave to create an endfire beam. Numerical analysis was used on various geometric aspects of this kind of antenna to find the most optimal results. Analyzing an analytical approach to the DSWA a tapering scheme based on the modified Hansen-Woodyard condition was applied to create the highest directivity.

## Table of Contents

Chapter 1 .....	1
1.1 Introduction .....	1
1.2 Previous Work .....	3
Chapter 2.....	7
2.1 Non-Tapered Cylindrical DRA .....	7
2.2 Tapered DSWA .....	7
2.3 HFSS Radiation Boundary .....	11
2.4 HFSS “Wedge” Model .....	12
Chapter 3.....	19
3.1 Dielectric Distribution .....	19
3.2 Individually Optimized Taper .....	29
3.3 Equation Based Dielectric Distribution .....	31
3.4 Probe Height .....	33
Chapter 4.....	38
4.1 Analytical Pattern Formation .....	38
4.2 Analytical Equation Validation .....	41
4.3 HFSS Modeling Based on the Hansen-Woodyard Condition .....	46
4.4 Solver Comparison .....	53
Chapter 5.....	56
5.1 Conclusion .....	56
References.....	59
Appendix A: Taper Distribution Equations .....	61
Appendix B: Matlab and Mathcad Program for Analytical Solution .....	64
Appendix C: HFSS Model Specifications based on HW Condition .....	67
Appendix D: Summary of DSWA Design Specifications .....	68

## List of Figures

Figure 1. Antenna geometry [1].....	2
Figure 2. Antenna feed configuration [1].....	2
Figure 3. Dielectric-rod antenna with linear taper [5]. .....	4
Figure 4. Design of optimized Teflon-based dielectric rod with a series of steps.....	4
Figure 5. Tapered cylindrical DSWA design.....	6
Figure 6. HFSS model of DSWA.....	6
Figure 7. Far field endfire E-field strength of surface wave vs. varying radii.....	8
Figure 8. Maximum magnitude plot of near-field E-field inside non-tapered cylinder DRA .....	8
Figure 9. Endfire directivity of the radiation pattern as the individual widths of the concentric rings increase.....	10
Figure 10. Polar plot of far-field pattern ( $E_\theta$ polarization) for a tapered ten ring structure having a ring width of 48.6 mm.....	10
Figure 11. Maximum magnitude plot of E-field inside tapered cylinder DRA .....	11
Figure 12. Top View of DSWA with tangential E-Field and H-Field shown. ....	13
Figure 13. Image theory for perfect magnetic boundary conditions.....	14
Figure 14. Top view of DSWA “wedge” structure with PMC walls, which maintains E- Field and H-Field integrity.....	15
Figure 15. Polar plot of far-field pattern ( $E_\theta$ polarization) for a tapered ten ring structure using the full model (red) vs. $10^\circ$ “wedge” model (blue) .....	15
Figure 16. Polar plot of far-field pattern ( $E_\theta$ polarization) for a tapered ten ring structure using a full model (red) vs. a $10^\circ$ “wedge” model with a -5.79 dB normalization factor	

(blue).....	16
Figure 17. An HFSS model of 10° “wedge” of ten ring DRA structure used to represent the 360° model .....	16
Figure 18. Quarter wavelength dipole radiation pattern from an HFSS model of 10° “wedge” (red) vs HFSS using a full 360° model (blue).....	18
Figure 19. TEN Model of the wave propagating from source to load inside DSWA.....	20
Figure 20. Normalized polar plot (in dB) of the far-field pattern ( $E_\theta$ polarization) for a tapered ten ring structure (red) vs. a tapered 19 ring structure (blue).....	21
Figure 21. Normalized polar plot (in dB) of the far-field pattern ( $E_\theta$ polarization) for a tapered structure with 20% change (black), 10% change (red), 9% change (blue), and an 8% change (orange). .....	23
Figure 22. Normalized polar plot (in dB) of the far-field pattern ( $E_\theta$ polarization) for tapered structures with a percentage change of 7.0% (black), 6.0% (red), 5.0% (blue), and 4.0% (orange).....	24
Figure 23. Normalized polar plot of far-field pattern ( $E_\theta$ polarization) for electrically modified 8.0% antenna (red) vs non-altered 8.0% antenna (blue) .....	25
Figure 24. Normalized polar plot of far-field pattern ( $E_\theta$ polarization) for a tapered structure with 6.0% (black), 5.0% (red), 4.0% (blue) and 3.0% (orange) .....	27
Figure 25. Normalized polar plot of far-field pattern ( $E_\theta$ polarization) for a 1% tapered structure with base $\epsilon_r=1.47 \cdot 10^0$ “wedge” (red) vs full scale model (blue) .....	28
Figure 26. Normalized polar plot of far-field pattern ( $E_\theta$ polarization) for a 1% tapered structure with base $\epsilon_r=1.47 \cdot 10^0$ “wedge” (red) vs full scale model with altered height (blue) .....	28

Figure 27. Normalized polar plot of far-field pattern ( $E_\theta$ polarization) linear taper (red) vs optimized taper (blue) using “wedge” model.....	30
Figure 28. Normalized polar plot of far-field pattern ( $E_\theta$ polarization) optimized taper full scale model (red) vs optimized taper “wedge” model (blue) .....	31
Figure 29. Normalized polar plot (in dB) of the far-field pattern ( $E_\theta$ polarization) for the linear taper (blue), cubic taper (purple), quadratic taper (green) and polynomial 4 <sup>th</sup> order (black) (left) and $\epsilon_r$ vs. ring distribution (right).....	32
Figure 30. Normalized polar plot (in dB) of the far-field pattern ( $E_\theta$ polarization) GP ( $\alpha = 6, n=3$ ) (blue), GP ( $\alpha = 1, n = 3$ ) (red), GP ( $\alpha = 1, n = 4$ ) (green) and ( $\alpha = 1, n = 5$ ) (purple) (left). $\epsilon_r$ vs. ring distribution (right).....	33
Figure 31. Directivity (in dB) for varying probe height at 2 GHz for DSWA with $\epsilon_r = 1.47$ with a 1% taper .....	35
Figure 32. Normalized Polar plot (in dB) of the far-field pattern ( $E_{el}$ polarization) for DSWA $\epsilon_r = 1.47$ with a 1% taper probe height 75mm (blue) vs probe height 65mm (red) .....	36
Figure 33. Directivity (in dB) vs. probe height for DSWA with $\epsilon_r = 4.6$ with a 4% taper .....	36
Figure 34. Total E-field (in dB) radiated at endfire for varying probe height 2 GHz for DSWA with $\epsilon_r = 4.6$ with a 4% taper.....	37
Figure 35. Matlab normalized plot (in dB) of the far-field pattern ( $E_{el}$ polarization) $\beta=k_0$ for $20\lambda_0$ radius structure .....	42
Figure 36. Matlab normalized plot (in dB) of the far-field pattern ( $E_{el}$ polarization) using $\beta = k_0 \sin(45^\circ)$ for a $20\lambda_0$ radius structure.....	42

Figure 37. Matlab normalized plot (in dB) of the far-field pattern ( $E_{el}$ polarization) for a non-tapered structure with $\beta = k_0$ for $3.27\lambda_0$ radius structure.....	43
Figure 38. Matlab normalized plot (in dB) of the far-field pattern ( $E_{el}$ polarization) for a tapered $3.27\lambda_0$ radius structure .....	43
Figure 39. Matcad normalized plot (in dB) of the far-field pattern ( $E_{el}$ polarization) for a linear tapered $3.27\lambda_0$ radius structure with maximum directivity .....	44
Figure 40. Mathcad normalized plot (in dB) of the far-field pattern ( $E_{el}$ polarization) for an exponential tapered $3.27\lambda_0$ radius structure with maximum directivity.....	45
Figure 41. Polar plot (in dB) of the far-field pattern ( $E_{el}$ polarization) for DSWA $\epsilon_r = 1.403$ and a 1% taper, with a height of 121mm and probe height 71mm .....	47
Figure 42. Polar plot (in dB) of the far-field pattern ( $E_{el}$ polarization) for DSWA $\epsilon_r = 1.402$ and a .1% taper with a height of 121mm and probe height 71mm .....	47
Figure 43. Polar plot (in dB) of the far-field pattern ( $E_{el}$ polarization) for a percent tapered DSWA of varied sizes $3.27\lambda_0$ (red), $4.5\lambda_0$ (black) and $10\lambda_0$ (blue), for a fixed $\beta$ .	50
Figure 44. $\beta$ vs. dielectric rings for optimized $0.46\lambda_0$ - $12.5\lambda_0$ DSWA linear tapered permittivity structures .....	50
Figure 45. Initial $\beta$ vs. radial size in $\lambda_0$ for a structure with an optimized linear taper in the permittivity .....	51
Figure 46. Directivity vs. radial size in $\lambda_0$ for a structure with an optimized linear taper in the permittivity.....	52
Figure 47. Height of substrate vs. radial size in $\lambda_0$ for a structure with an optimized linear taper in the permittivity.....	52
Figure 48. Beamwidth vs. radial size in $\lambda_0$ of structure with an optimized linear taper in	

the permittivity.....53

Figure 49. CST full model with a finite ground plane (black), HFSS “wedge” model with a finite ground plane (red), and an HFSS “wedge” model with an infinite ground plane (blue).....55

## List of Tables

Table 1. Dielectric distribution of each ring of 10-ring vs 19-ring antenna .....	20
Table 2. Dielectric distribution and base dielectric change from 20% - 8% tapers .....	22
Table 3. Dielectric distribution and base dielectric change from 7% - 4% tapers .....	23
Table 4. Antenna model with an 8.0% taper compared to electrically modified model and original model with matching $h/\lambda_d$ heights .....	25
Table 5. Dielectric distribution with fixed base dielectrics and varying percent reductions with increasing outer ring dielectrics .....	26
Table 6. Dielectric distribution for 1% tapered DSWA.....	28
Table 7. Optimization results for individual ring permittivity analysis vs. a linear taper model.....	30
Table 8. Dielectric distribution summary table with comparison of beam width, side lobe level, and directivity.....	34
Table 9. Analytical tapering analysis for highest directivity obtained for $3.27\lambda_0$ structures compared to $\beta_{HW}$ .....	46
Table 10. DSWA with varying percent tapers and a comparison to the $\beta_{AVG}$ and $\beta_{HW}$ .....	49
Table 11. DSWA with linear permittivity tapers and a comparison to the $\beta_{AVG}$ and $\beta_{HW}$ .....	49

# Chapter 1

## 1. Introduction

Dielectric resonator antennas (DRAs) are emerging as a new and viable alternative to conventional low-gain elements, such as dipoles, monopoles, and microstrip patches since their discovery in the 1980's [1]. A DRA is a dielectric structure typically with a high relative permittivity ( $10 < \epsilon_r < 100$ ) that when properly excited, usually by a probe or a microstrip feed line, creates a cavity mode resonance. When compared to the popular microstrip antenna, DRAs have less ohmic loss and have a higher bandwidth. However, they cannot usually be fabricated by conventional photolithography [2]. They have been growing in popularity, and there are numerous designs that vary in shape, permittivity, and feed configuration, as well as combinations involving other types of antennas.

One of the earliest shapes used as a DRA is that of a circular cylinder. Such a DRA is usually placed on a metallic ground plane with a probe inserted off-center near the edge to excite the dominant  $TM_{110}$  mode [1]. An example of the DRA antenna geometry can be seen in Figure 1 with its feed configuration shown in Figure 2. Various other higher-order resonant modes can also be excited. The DRA is not a perfect cavity; there are fringing fields and radiation leakage from the surface, which in fact make it useful as an antenna element [2].

Usually broadside patterns with nearly omnidirectional E-plane patterns are desired. However, power can sometimes radiate horizontally and create unwanted lateral radiation along the ground plane. This lateral radiation will corrupt the overall radiation

pattern and will increase mutual coupling between other antennas if they are elements in an array. Significant studies have been taken to reduce these effects [3].

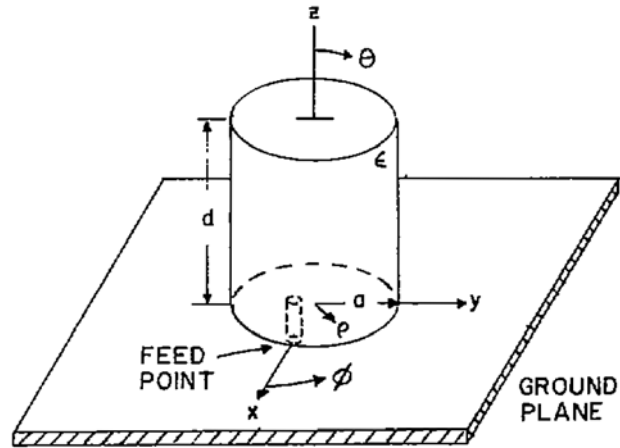


Figure 1. Antenna geometry [1].

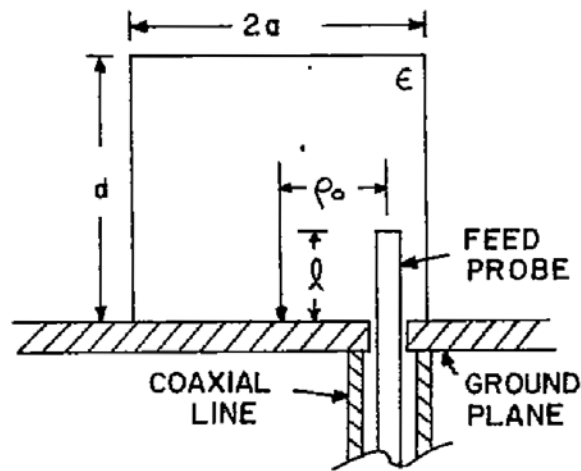


Figure 2. Antenna feed configuration [1].

In the following research a variation of a cylindrical DRA will be explored that acts as a dielectric surface-wave antenna (DSWA), with the objective of enhancing lateral

radiation in order to create azimuthally omnidirectional directive endfire radiation along the horizon. This is achieved by exciting the cylindrical DSWA in the center with a vertical probe and radially tapering the relative permittivity from a larger value at the center to a smaller value at the edge.

It is well known that surface-wave antennas can be utilized to obtain directive end-fire radiation patterns [4]. Often the shape of the antenna is in the form of a tapered rod, which can be used to produce a pencil beam at endfire, but other interesting shapes have been explored to achieve other beam shapes [3-13].

## **2. Previous Work**

One of the first dielectric-rod antennas studied in the 1950's had a uniform wall thickness with a linear taper design as seen in Figure 3 [5]. Studies in the 1970's involved optimizing this dielectric-rod profile with a series of step-down taper methods [6]. A modern day example of a working dielectric rod made of Teflon is a cylindrical structure with a step down cylindrical taper and a linear taper as shown in Figure 4 [7]. Most dielectric rods typically have electrical lengths of  $8\lambda_0$  or more. Studies showed that the dielectric rod could be a viable alternative to feed horns used in parabolic reflector antennas based on their radiation patterns, gain, and beamwidth [7]. The peak gain achieved by the optimized Teflon dielectric rod was 15 dB with a beamwidth of  $20^\circ$ . Higher gains can be achieved but are usually limited to about 20 dB [6]. Gains near this level can be achieved, but not without significantly increasing the already electrically large structures. The problem that appears is that there is significant radiation leakage from the sides which does not contribute to the strength of the endfire field.

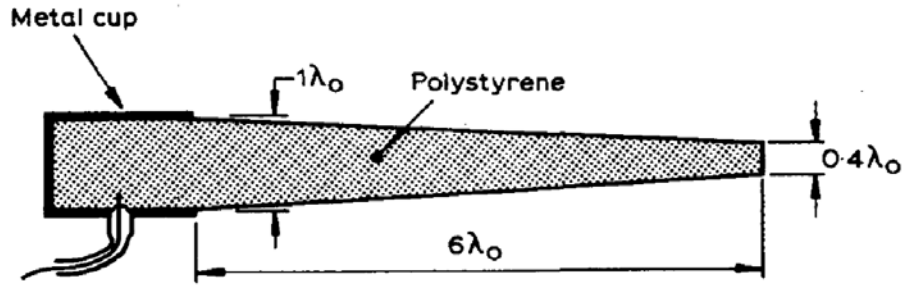


Figure 3. Dielectric-rod antenna with linear taper [5].

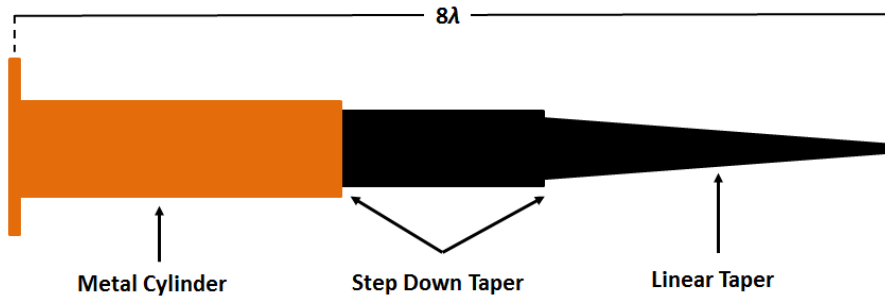


Figure 4. Design of optimized Teflon-based dielectric rod with a series of steps.

A cylindrically-tapered structure can produce an omnidirectional endfire beam. The dominant  $TM_0$  surface wave that propagates radially outward from the center is used to form the beam. A vertical probe at the center is used to launch the  $TM_0$  surface wave, which produces an aperture field that radiates an  $E_\theta$  polarized field. Simulations show that a strong standing wave field is created within a cylindrical structure of fixed height when only a single permittivity is used, regardless of the radius of the structure, due to reflections from the outer boundary. Therefore, a tapered structure is necessary to achieve a radially-propagating traveling surface wave. Tapering is achieved here by varying the

permittivity. This may be achieved in practice by drilling holes in the dielectric material or by milling thin air rings to create a smaller effective permittivity.

It is well known that the radiation from a very long tapered surface-wave structure, over which the reactance changes slowly, is expected to yield a directive endfire pattern [4]. The same concept is applied here to a cylindrically-tapered structure. Based on this concept, a tapered structure using ten homogeneous concentric rings with decreasing relative permittivity values was simulated in HFSS. The rings were chosen to have uniform intervals, so that the width of each dielectric ring is the same. This gradual tapering of the permittivity allows for a radially-traveling surface wave along the structure. Figure 5 shows one particular design. The cylindrical structure is excited at a frequency of 2.0 GHz with a probe feed, and the structure sits on an infinitely large, perfect electric conductor (PEC) ground plane. The relative permittivity varies in integer steps from 10.0 at the center to 1.0 at the outer ring, to allow for a smooth transition to free space for the traveling surface wave. Figure 6 shows a perspective view of the model as simulated in HFSS. Initial results showed an E-field strength at the surface of about 19 dB with a directive gain of 13 dB. Numerous optimization techniques using HFSS and analytical analysis will be used to shape the beam for increased directivity, while keeping side lobe levels in the range of -10 dB to -13 dB, as seen in the following chapters. The end goal will be to create a generalized design table for optimizing a DSWA based on frequency and desired radial size of the antenna to achieve the best performance.

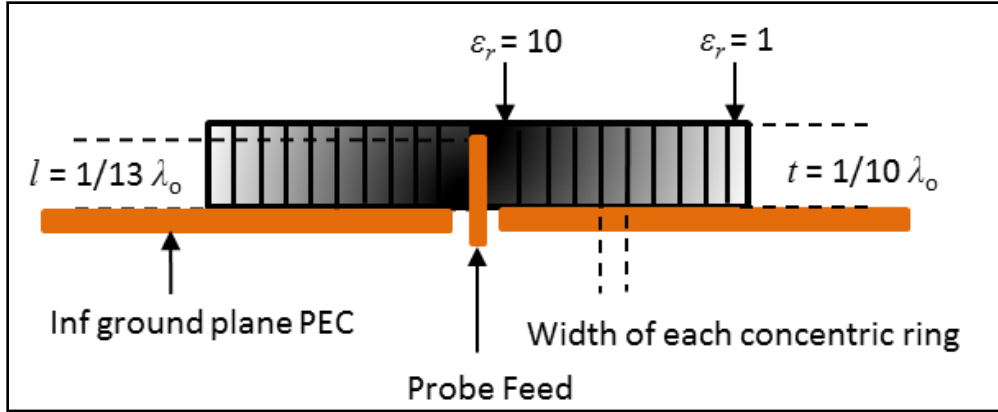


Figure 5. Tapered cylindrical DSWA design.

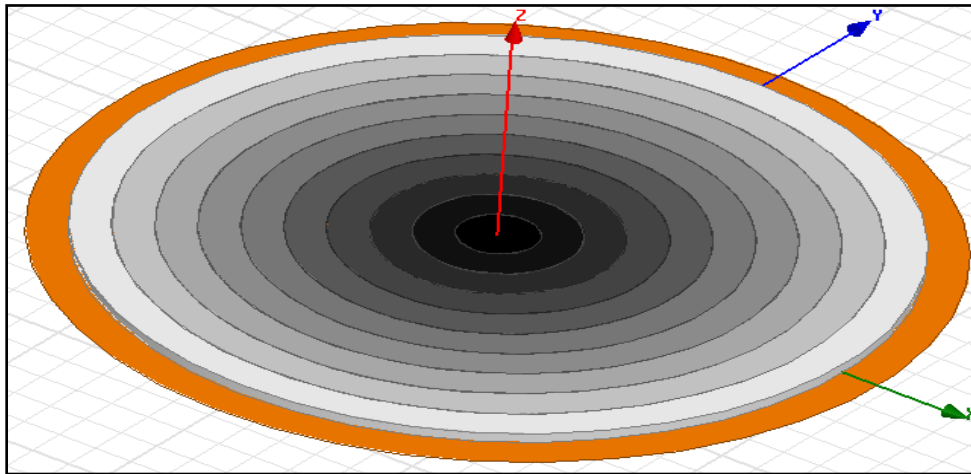


Figure 6. HFSS model of DSWA.

## Chapter 2

### 1. Non-Tapered Cylindrical DRA

Initially, non-tapered DRA models were investigated with varying radii to determine potential ways to increase surface-wave directivity. Simulations involved a low-profile, non-tapered DRA ( $\epsilon_r = 10$ ), center fed with a probe over a ground plane with varying radii. As the radii increased, the directivity of the surface wave was expected to increase as well; however, this was not the case. Figure 7 shows the E-field surface wave strength plotted vs. varying radii. The E-field strengthened and peaked when the radii was chosen to be an integer multiple of  $0.5\lambda_d$ . These initial results gave an indication that a traveling wave was not being supported, but rather a standing wave was produced. This was not the intent, since a traveling wave was desired. Figure 8 shows the magnitude of the E-field inside the DRA from the center of the probe ( $\rho = 0$  mm) to the outer radius ( $\rho = 95$  mm). The E-field in the cylindrical DRA peaks at both  $\rho = 40$  mm and  $\rho = 70$  mm, which clearly confirms a standing wave. This wave is present in all similar structures with varying radii. Therefore, only varying the radii was not effective in increasing the directivity of the beam; thus, tapered structures were investigated.

### 2. Tapered DSWA

It is well known that the radiation from a very long tapered surface-wave structure, over which the reactance changes slowly, is expected to yield a directive endfire pattern [4]. The same concept is applied here to a

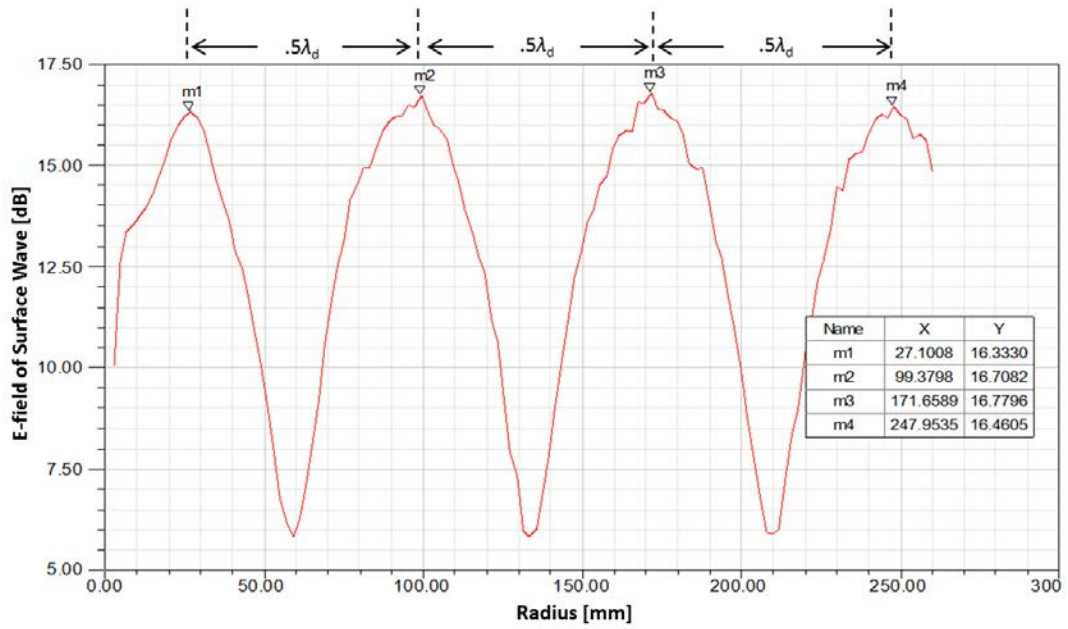


Figure 7. Far field endfire E-field strength of surface wave vs. varying radii.

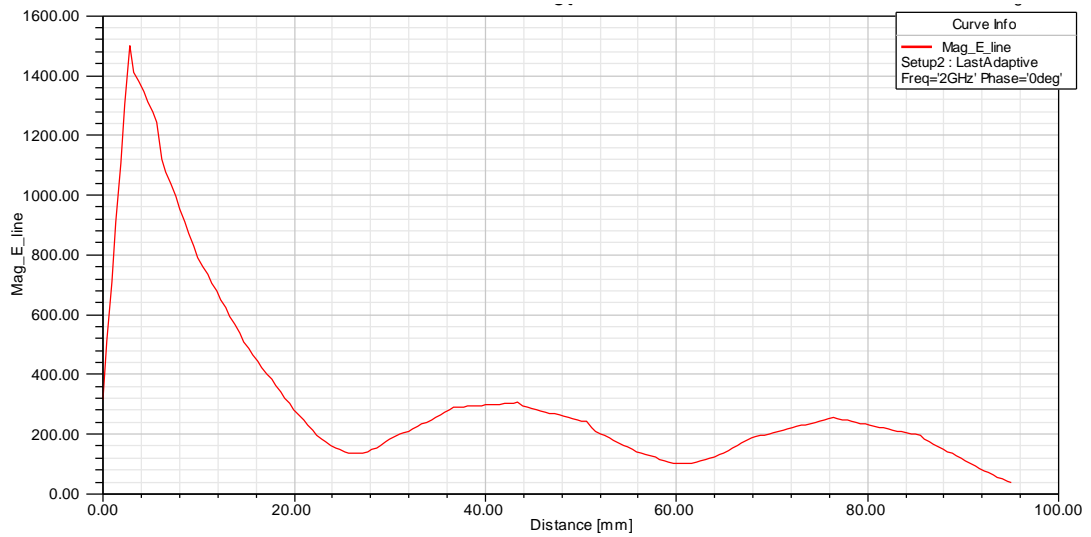


Figure 8. Maximum magnitude plot of near-field E-field inside non-tapered cylindrical DRA.

cylindrically-tapered structure. Based on this concept, a tapered structure using ten homogeneous concentric rings with decreasing relative permittivity values was simulated in HFSS. The rings were chosen to have uniform intervals, so that the width of each dielectric ring is the same. This gradual tapering of the permittivity allows for a radially-traveling surface wave along the structure. The previously shown design can be seen in Figures 5 and 6. The cylindrical structure is excited at a frequency of 2.0 GHz with a probe, and the structure sits on an infinite PEC ground plane. The relative permittivity varies in integer steps from 10.0 at the center to 1.0 at the outer ring, to allow for a smooth transition to free space for the traveling surface wave.

The width of each concentric ring was varied from 20 mm to 120 mm. As the rings are collectively increased in size the overall radius of the structure increases; hence, there is a more gradual spatial tapering of the permittivity, which results in an increase in the directivity of the pattern, as seen in Fig 9. In the next design, a somewhat arbitrary value for the width of each of the ten concentric rings was chosen to be 48.6 mm, with the relative permittivity varying in integer steps from 10.0 at the inner ring to 1.0 at the outer ring. The radiation plot shows a very strong directive beam for  $E_{el}$  at  $90^\circ$  as seen in Figure 10. The E-field inside the DRA was plotted to verify that a strong traveling wave was being supported. Figure 11 shows the E-field strength vs. the radius from the center of the structure to the outer edge. An expected gradual decrease in the E-field can be seen, which has no peaks resembling the standing wave previously seen in Figure 8. This clearly confirms that a traveling wave is supported. There are slight increases in the E-field at the concentric ring interfaces of the structure. Further analysis will investigate if removing these slight peaks has an effect on the surface waves.

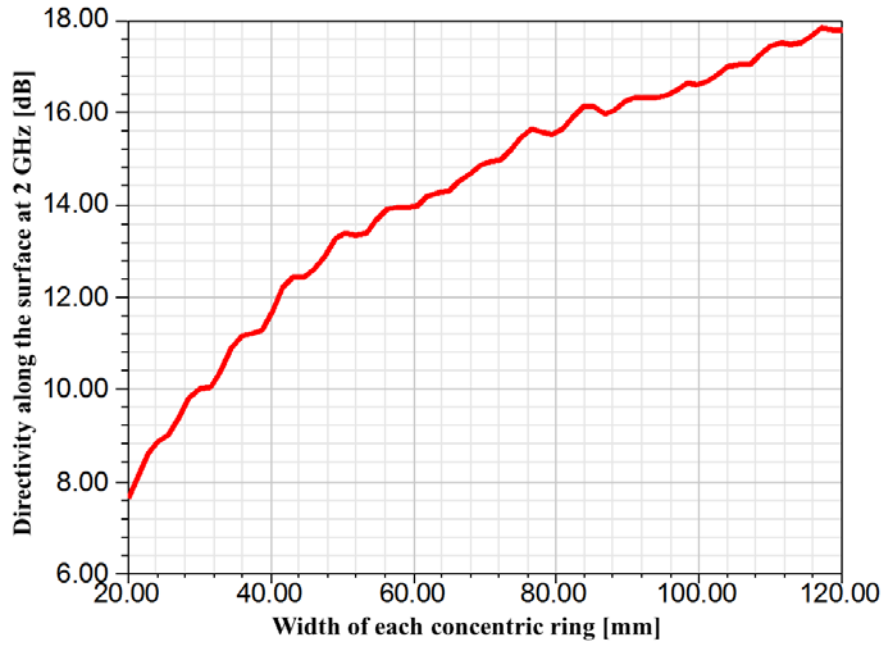


Figure 9. Endfire directivity of the radiation pattern as the individual widths of the concentric rings increase.

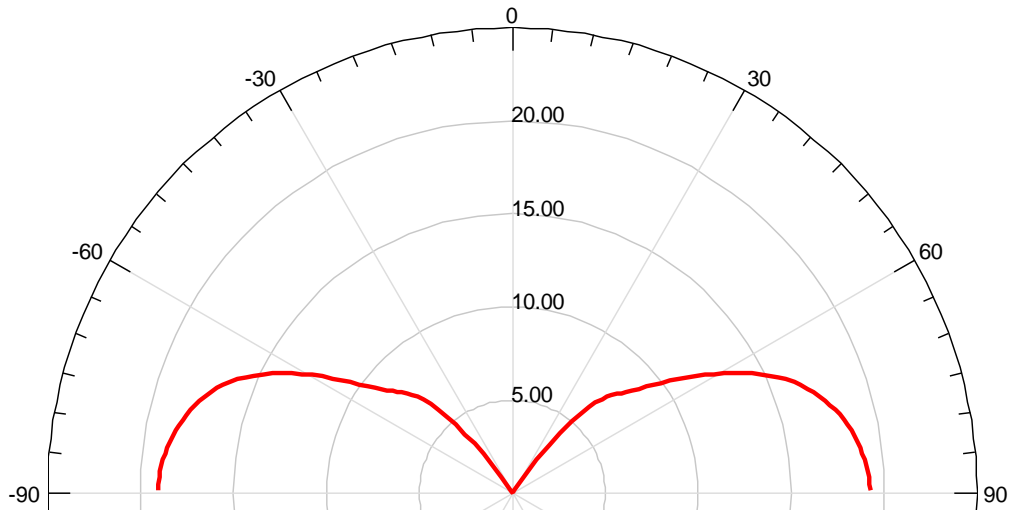


Figure 10. Polar plot of far-field pattern ( $E_{el}$  polarization) for a tapered ten ring structure having a ring width of 48.6 mm.

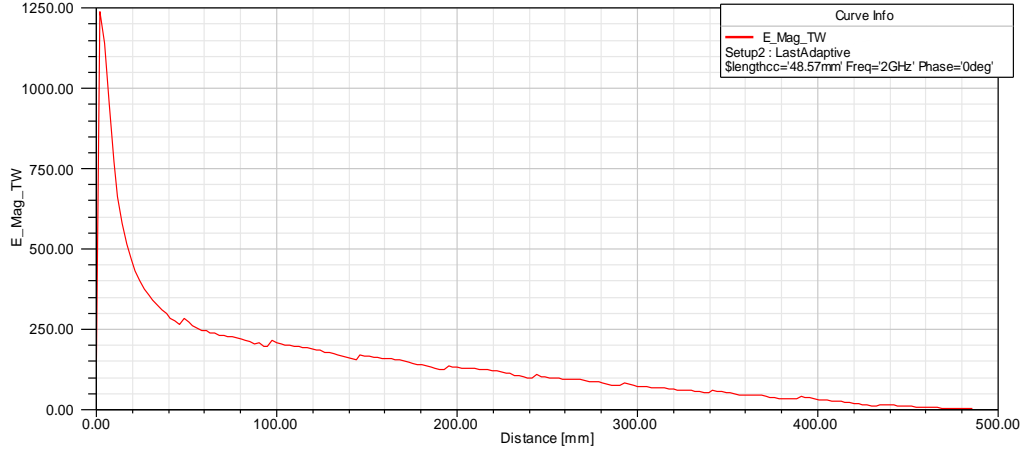


Figure 11. Maximum magnitude plot of E-field inside tapered cylinder DRA.

### 3. HFSS Radiation Boundary

Theory states that a larger and more gradually tapered structure produces stronger directive radiation in the  $\theta = 90^\circ$  direction [4-6, 10, 12-13]. However, initial HFSS tapered structures showed just the opposite, with strong directive gain near  $\theta = 0^\circ$ . After multiple troubleshooting attempts to validate the model it was suspected that the radiation boundary was the problem. A typical cylindrical radiation boundary was initially used and offset from the DRA by the generally approved spacing of  $0.25\lambda_0$ . This offset is typically used in most antenna models but was not sufficient for the DSWA model. The DSWA is electrically much larger in the radial direction than the vertical direction. The fields were hitting the top of the radiation boundary much sooner and with stronger field strength than the distant surface boundary of interest where the surface waves were transitioning to free space. Therefore the radiation boundary was changed from a cylinder to a half hemispherical radiation boundary, which successfully overcame these faulty radiation effects. To verify these results were accurate the cylindrical boundary

was also expanded to have similar distances in the vertical and horizontal planes, which also produced successful results identical to the spherical boundary. The desired results were achieved showing strong directivity at the surface with minimal E-field strength at  $\theta = 0^\circ$ . The cylindrical boundary was much larger in volume than the spherical boundary and was therefore discarded to reduce the simulation time required.

#### **4. HFSS “Wedge” Model**

The first challenge to performing optimization techniques was to drastically reduce the simulation time required for the large DSWA. As previously discussed, the hemispherical radiation boundary requires a large volume that needs to be meshed for each simulation. This additional volume increased the computational time to several hours per simulation. This limitation was unacceptable due to the anticipated optimization of the tapered structure where multiple simulation results would be needed quickly.

Since the structure is a body of revolution and the nature of the fields is azimuthally omnidirectional, smaller sections could be used to simulate the entire structure. Figure 12 shows a top view of a cylindrical DRA with the  $TM_0$  surface-wave mode having a radially-directed outward propagating tangential E-field launched from the centered probe and an azimuthally-directed radially propagating tangential H-field. Because of the symmetry, image theory can be used to drastically reduce simulation time and to decrease the size of the structure being analyzed. This structure allows for the E and H fields to be continuously reproduced using perfect magnetic boundary conditions (PMC) as seen in Figure 13. The parallel E-field and normal H-field to the plane are

maintained across the PMC boundary.

Quarter “wedge” models were initially investigated which involved two perpendicular planes of symmetry which act as a PMC. This setup cut simulation time to less than an hour per simulation. Although improvements in performance were achieved, the required simulation time was still not ideal.

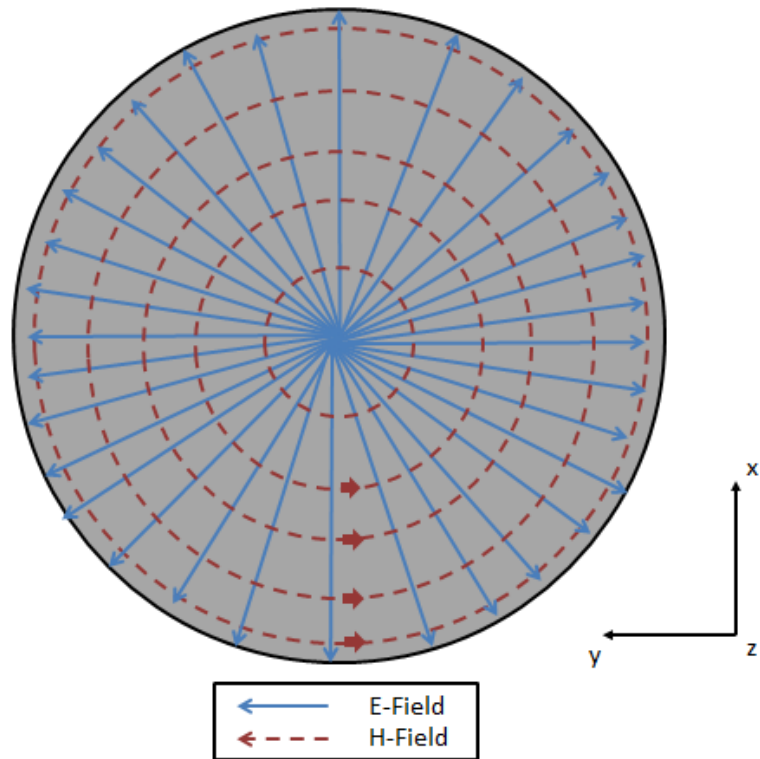


Figure 12. Top View of DSWA with tangential E-Field and H-Field shown.

The smaller “wedge” seen in Figure 14 was next simulated using no planes of symmetry but only magnetic side walls. The fields are completely maintained with only a fraction of the structure needing to be analyzed. The fields used in the analysis can only be used in half of one plane centered inside the radiation boundary ( $\phi = 0^\circ$ ,  $0 < \theta < 90^\circ$ ). This plane will cut directly in the center of the wedge and will be used for all further analysis.

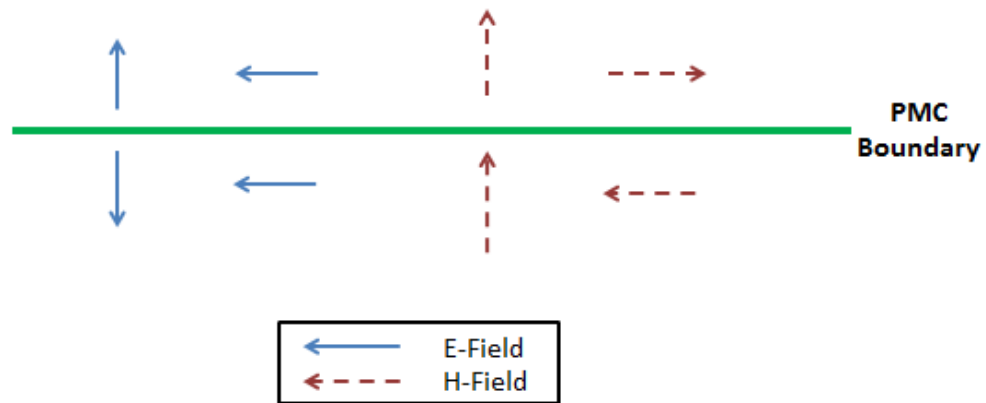


Figure 13. Image theory for perfect magnetic boundary conditions.

The simulation of a uniform ten ring structure having a  $10^\circ$  “wedge” was compared to the complete  $360^\circ$  10 ring structure, and reliable results were found. The only significant difference was the increase in field strength of 5.79 dB as seen in Figure 15. Therefore a normalization factor of -5.79 dB was added to correct the pattern in Figure 16. After this correction there are only small field pattern differences of less than 0.4 dB in certain areas of the plot of the  $10^\circ$  “wedge” model. Therefore the  $10^\circ$  “wedge” HFSS model as seen in Figure 17 was used in all further simulations.

It is not clearly evident why there is a difference in the two field strengths of these two models. Theory indicates that there should not be any difference. However, it is suspected that the wedge radiation boundary could be negatively manipulating the E-field strength or some other HFSS error is present. This model manipulation did successfully shorten simulation times from an hour to less than 2-3 minutes, while providing reliable pattern results.

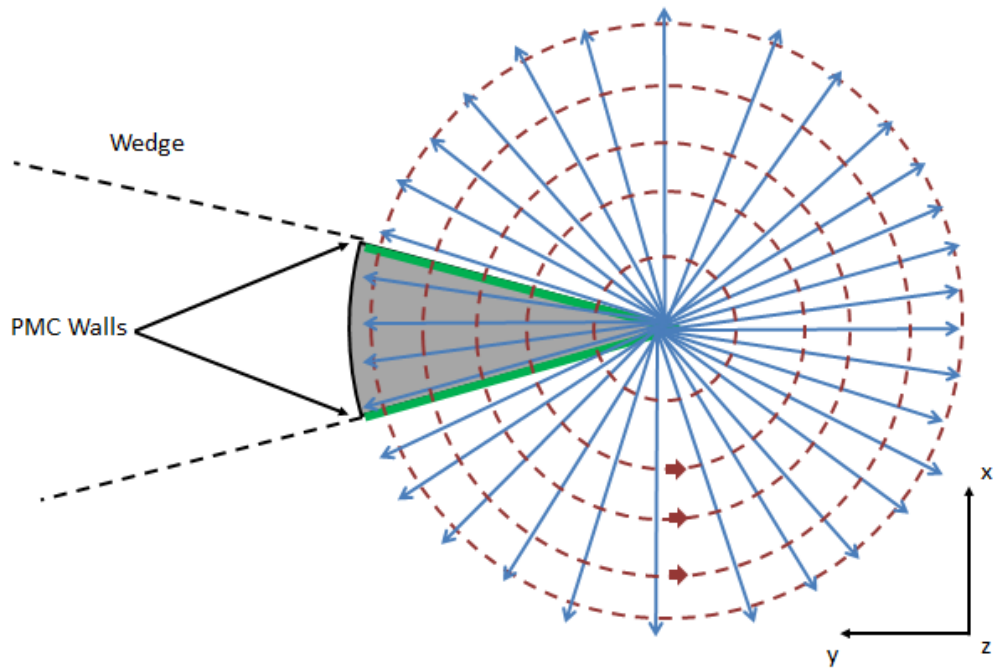


Figure 14. Top view of DSWA “wedge” structure with PMC walls, which maintains E-Field and H-Field integrity.

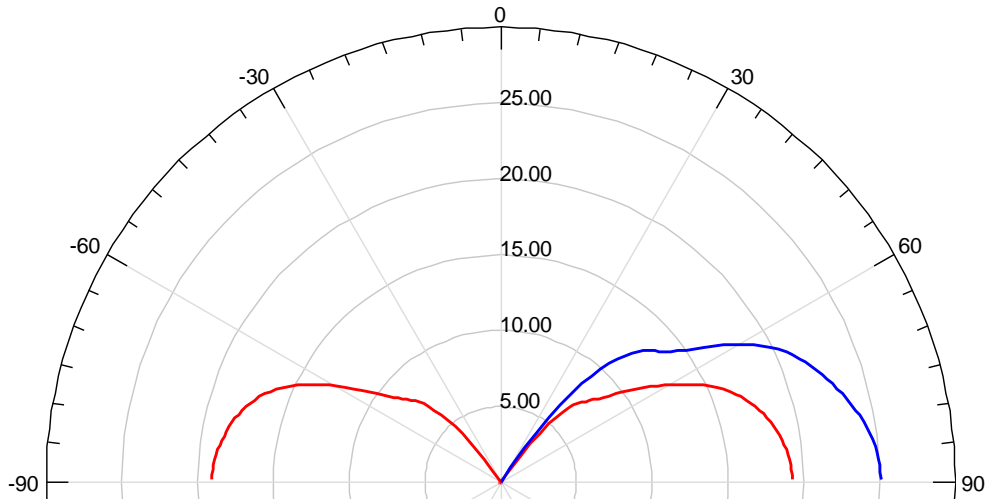


Figure 15. Polar plot of far-field pattern ( $E_{el}$  polarization) for a tapered ten ring structure using the full model (red) vs. the  $10^\circ$  “wedge” model (blue).

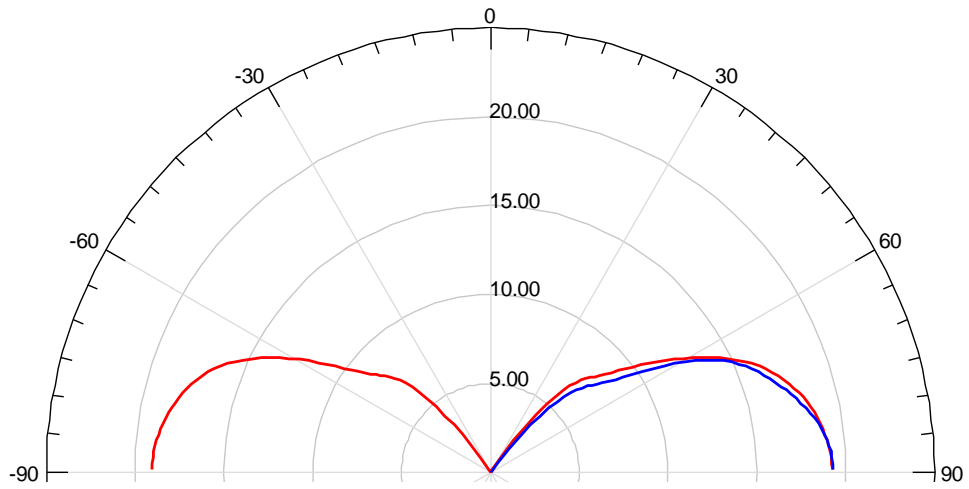


Figure 16. Polar plot of far-field pattern ( $E_{el}$  polarization) for a tapered ten ring structure using a full model (red) vs. a  $10^\circ$  “wedge” model with a -5.79 dB normalization factor (blue).

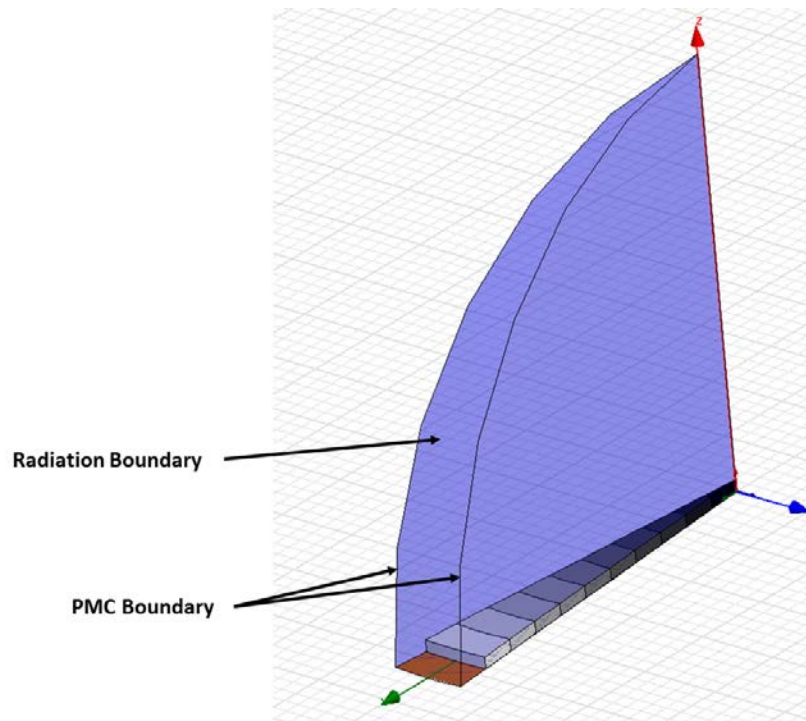


Figure 17. An HFSS  $10^\circ$  “wedge” model of a ten ring DRA structure used to represent the  $360^\circ$  model.

One failure that was noted towards the end of this research was that the  $10^\circ$  “wedge” HFSS model does give a significant radiation pattern error when the dielectric constant of the rings become extremely low ( $\epsilon_r \approx 1$ ) or if the rings are removed completely. An example of this is illustrated in Figure 18 where there are no rings and the radiation pattern is directly from the probe, which is being used as a monopole. The full HFSS model has an expected broadside omnidirectional radiation pattern over an infinite ground plane. However, the  $10^\circ$  “wedge” model has an unexpected higher directivity with a HPBW  $16^\circ$  difference from the full model. Distortions in the radiation pattern become evident as the full model is sliced and becomes progressively worse as the angle of the wedge model decreases. Fortunately, this distortion has little effect on the various DSWA designs, as will be seen later on. In all cases the HPBW is not distorted and only certain regions are effected,  $0 < \theta < 45^\circ$ , where side lobes are generally low. Most of the results given later include the full scale model for verification. The “wedge” model is simply a tool for quick optimization and faster simulation times, which proves useful for this purpose. It is also important to understand these distortions also vary based on the electrical size of the ground plane and radiation boundary of the “wedge” model. As the ground plane becomes larger in radius for a single probe with no dielectric rings the directivity and E-field gradually increase. The reason for this is also unknown since the ground plane is considered an infinite PEC, which connects directly to the radiation boundary. No other changes besides radius are being made to the model. When similar comparisons are made on a full scale model of a single probe with no dielectric rings, the values for directivity and E-field values fluctuate randomly within 1-3% and hence are assumed to be fairly reliable. Based on these model simulations, full scale

model values are used for most models with radii less than  $4\lambda_0$ . Extrapolated data for smaller antennas will be used for estimated error correction for antennas that are larger. A single probe with varied ground plane radii is not a good baseline model for directivity, HPBW, or E-field baseline corrections. The DSWAs are more complicated, naturally more directive, and do not suffer from such severe errors as are seen in the single-probe model. Therefore, as a general warning, directivities given here should be used as a reference and not explicitly for design purposes. These inadequacies for design purposes will not be fully addressed in this thesis due to time constraints. They will, however, be addressed in future work.

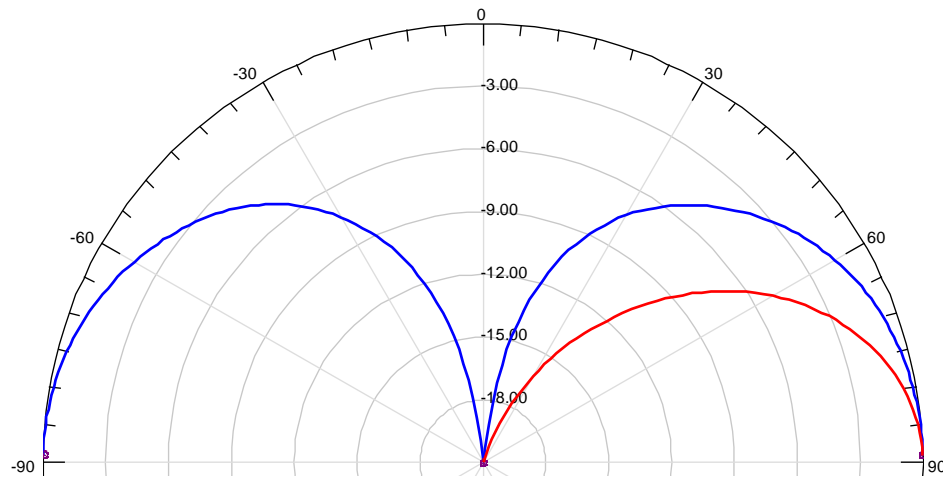


Figure 18. Quarter wavelength dipole radiation pattern from an HFSS model using a  $10^\circ$  “wedge” (red) vs. HFSS using a full  $360^\circ$  model (blue).

## Chapter 3

### 1. Dielectric Distribution

The theoretical solution of these tapered structures is difficult because the radiation does not emanate from a simple plane aperture as is the case with a metallic horn [6]. Many isolated aspects of this problem have been successfully analyzed, until the overall radiation system can be treated as a whole, the optimization of these antennas rests largely with experimental information [6]. Therefore numerical analysis with HFSS will initially be used by varying the number of steps in the dielectric, the dielectric distribution within the structure, the individual ring widths, and the substrate height.

It is useful to understand that the plane waves inside the tapered structure can be modeled using the Transverse Equivalent Network (TEN) model. The current is represented by the H-field and the voltage represented by the E-field seen in Figure 19. Each ring has its own impedance value; and as the TM wave propagates away from the source, it has reflections at each interface. The field strength is gradually diminished. Therefore, it is important to keep these reflections as small as possible so the highest transmitted field can pass through to create a strong radiated field at the load. Smaller percentage changes in taper variations in the dielectric will be compared in further analysis and simulations. It is expected that a DSWA that has the most gradual of tapers will have more directive endfire beams. The Transverse Resonance Equation (TRE) can also be used to calculate the wavenumber of the  $TM_0$  surface-wave mode and the impedance, reflection and transmission at each section, if needed.

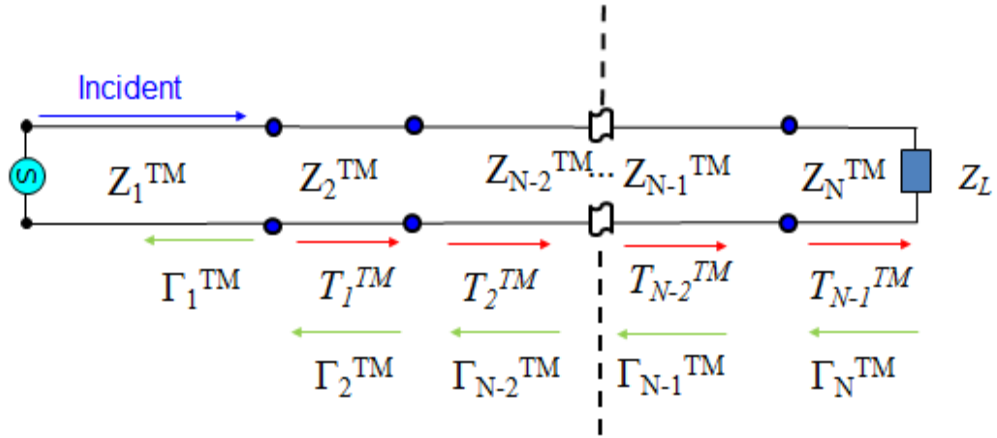


Figure 19. TEN model of the wave propagating from a source to a load on the DSWA.

The first variable of interest was the number of dielectric rings, which would represent the number of steps in the tapered dielectric antenna. The initial ten ring antenna ( $1 < \epsilon_r < 10.0$ ) with an equal ring width example was compared to a 19 ring antenna ( $1 < \epsilon_r < 10.0$ ) with overall radius being equal to that of the ten ring antenna. Values can be seen in Table 1. The normalized far-field pattern ( $E_{el}$  polarization) of the two antennas can be seen in Figure 20. No noticeable difference can be seen between the two except for a slightly smoother main lobe with a slight increase in field strength at  $\theta = 70^\circ$  and a slight decrease of less than 1 dB at  $\theta = 50^\circ$ . Therefore, increasing the number of rings will result in a continuously smoother radiation pattern. However, later models with much sharper beam shapes and longer electrical lengths will require more rings to reduce sidelobe levels.

Table 1. Dielectric distribution of each ring for the 10-ring and 19-ring antennas.

	Ring (inner-outer)	1	2	3	4	5	6	7	8	9	10	11	12	13	14	15	16	17	18	19
10-ring	$\epsilon_r$	10	9	8	7	6	5	4	3	2	1									
19-ring	$\epsilon_r$	10	9.5	9	8.5	8	7.5	7	6.5	6	5.5	5	4.5	4	3.5	3	2.5	2	1.5	1

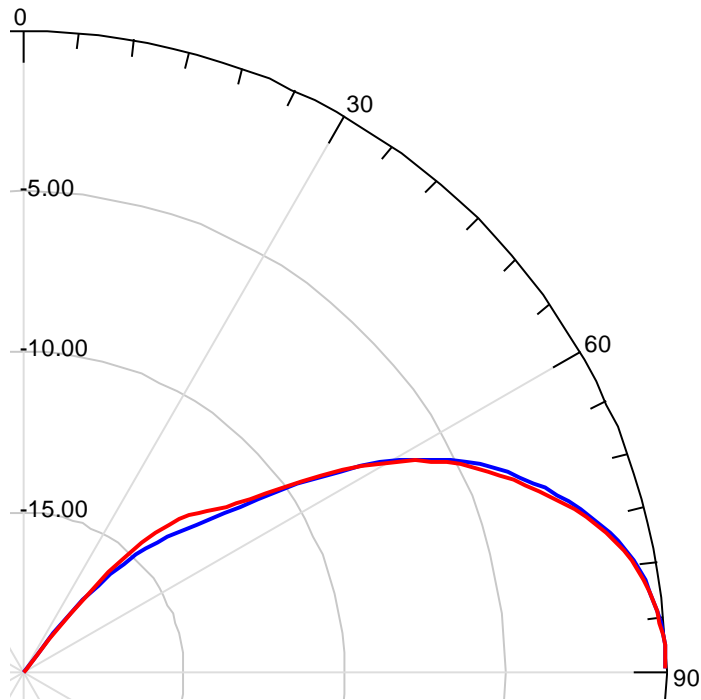


Figure 20. Normalized polar plot (in dB) of the far-field pattern ( $E_{el}$  polarization) for a tapered ten ring structure (red) vs. a tapered 19 ring structure (blue).

The next variable of interest was the dielectric distribution within the dielectric structure. Although a specified antenna radius is used, the ultimate goal is to find what kind of taper will optimize the directivity of the antenna regardless of its physical size. Based on the TEN model, lower base dielectrics that are naturally tapered more gradually to air ( $\epsilon_r = 1.0$ ) are predicted to create a more directive beam and have decreased reflections at each ring-to-ring interface. Simulated values can be seen in Table 2. The number of rings was set initially at 22 with the center dielectric having  $\epsilon_r = 10.0$ , with a reduction in  $\epsilon_r$  of 10% in each subsequent ring. The final outer ring is kept as close to  $\epsilon_r = 1$  as possible. As the percentage of  $\epsilon_r$  reduction decreases from 10% to 1% the number of required rings will naturally greatly increase. This change alone as seen from the

previous simulation would only create a continuously smoother radiation pattern. Therefore to create a varied dielectric distribution, the base dielectric will be varied in conjunction with the percentage change per ring to achieve the desired end permittivity that is near  $\epsilon_r = 1$ .

Table 2. Dielectric distribution and base dielectric change for 20% – 8% tapers.

% Change from each ring to ring interface	Ring	1	2	3	4	5	6	7	8	9	10	11	12	13	14	15	16	17	18	19	20	21	22
20%	$\epsilon_r$	8.00	6.40	5.12	4.10	3.28	2.62	2.10	1.68	1.34	1.07	1.00											
10%		10.00	9.00	8.10	7.29	6.56	5.90	5.31	4.78	4.30	3.87	3.49	3.14	2.82	2.54	2.29	2.06	1.85	1.67	1.50	1.35	1.22	1.09
9%		7.50	6.83	6.21	5.65	5.14	4.68	4.26	3.88	3.53	3.21	2.92	2.66	2.42	2.20	2.00	1.82	1.66	1.51	1.37	1.25	1.14	1.03
8%		5.80	5.34	4.91	4.52	4.16	3.82	3.52	3.24	2.98	2.74	2.52	2.32	2.13	1.96	1.80	1.66	1.53	1.41	1.29	1.19	1.09	1.01

The normalized far-field pattern ( $E_{el}$  polarization) of the four antennas can be seen in Figure 21. As the base dielectric and percentage change decreases, the directivity increases. There is a  $2.5^\circ$  drop in the half-power beamwidth (HPBW) from  $19.0^\circ$  to  $16.5^\circ$  from a reduction factor of 20% to 8%, respectively. There is also an uncharacteristic side lobe visible with the 8% dielectric distribution antenna. This due to the fact that the substrate height and probe length remain fixed and are becoming electrically smaller since  $\lambda_d$  is increasing as  $\epsilon_r$  decreases from 10.0 to 5.8.

Additional reflection factors of 7.0% – 4.0% are also compared in Table 3, with the results shown in Figure 22. The best taper for the comparison in this plot is 7%, which has the smallest HPBW at  $17.0^\circ$ . The lower percentage change antenna HPBW uncharacteristically starts to increase for this model. Consequently, the ideal taper has been found for this particular model with a fixed dielectric height of 14.8 mm, and it corresponds to the 6.0% percentage change antenna with HPBW of  $16.5^\circ$  from the

previous simulation. This concept, which will be shown again, clearly indicates that there is an ideal dielectric height for each type of antenna to create the smallest HPBW and a side lobe level less than or equal to -10.0 dB. In addition, the more gradual the tapering is, the smaller the HPBW will become.

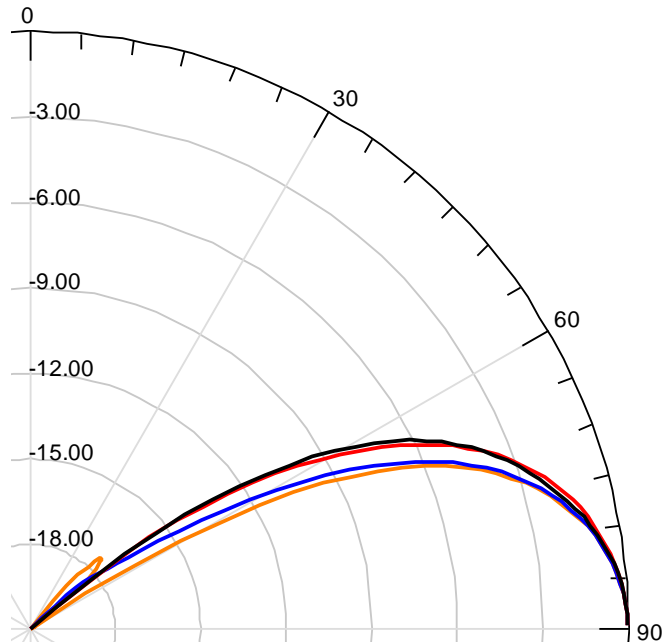


Figure 21. Normalized polar plot (in dB) of the far-field pattern ( $E_{el}$  polarization) for a tapered structure with 20% change (black), 10% change (red), 9% change (blue), and an 8% change (orange).

Table 3. Dielectric distribution and base dielectric change for 7% – 4% tapers.

% Change from each ring to ring interface	Ring	1	2	3	4	5	6	7	8	9	10	11	12	13	14	15	16	17	18	19	20	21	22
7%	$\epsilon_r$	4.60	4.28	3.98	3.70	3.44	3.20	2.98	2.77	2.57	2.39	2.23	2.07	1.93	1.79	1.67	1.55	1.44	1.34	1.25	1.16	1.08	1.00
6%		3.70	3.48	3.27	3.07	2.89	2.72	2.55	2.40	2.26	2.12	1.99	1.87	1.76	1.66	1.56	1.46	1.37	1.29	1.21	1.14	1.07	1.01
5%		3.00	2.85	2.71	2.57	2.44	2.32	2.21	2.10	1.99	1.89	1.80	1.71	1.62	1.54	1.46	1.39	1.32	1.25	1.19	1.13	1.08	1.02
4%		2.40	2.30	2.21	2.12	2.04	1.96	1.88	1.80	1.73	1.66	1.60	1.53	1.47	1.41	1.36	1.30	1.25	1.20	1.15	1.11	1.06	1.02

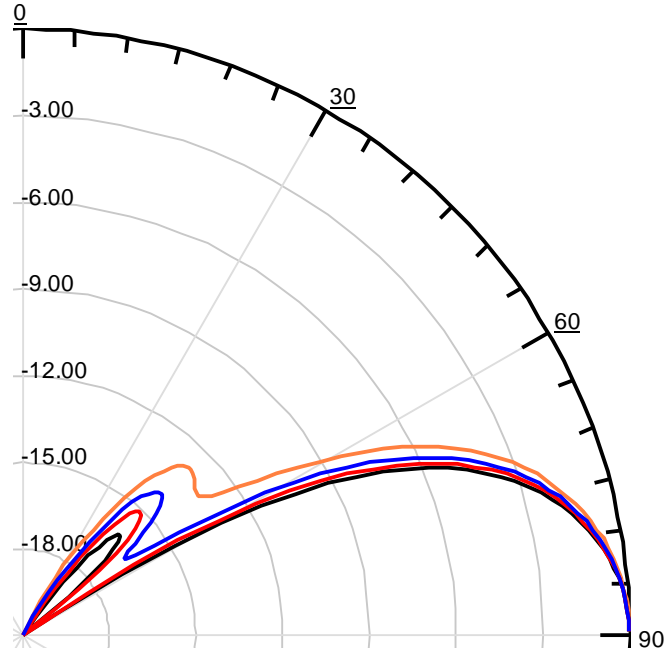


Figure 22. Normalized polar plot (in dB) of the far-field pattern ( $E_{el}$  polarization) for tapered structures with a percentage change of 7.0% (black), 6.0% (red), 5.0% (blue), and 4.0% (orange).

To ensure that the optimal probe and substrate heights were being used, the probe and the substrate height for the 8.0% change antenna, which had the most directive results, was then electrically increased in proportion to the height of the 10% change antenna model. This was done so that the height of the substrate will shift from  $h/\lambda_d = 0.13$  to 0.10, which was previously used in the original 10% antenna model. However, in this analysis a lower base dielectric will be used as seen in Table 4.

The probe height for the 8.0% change antenna is 11.82 mm with a substrate height of 14.8 mm. The electrically modified 8% change antenna has a probe height of 15.52 mm and a substrate height of 19.4 mm for base dielectric  $\epsilon_r = 5.8$ . The normalized far-field patterns ( $E_{el}$  polarization) shown in Figure 23 of the two antennas with a 8.0% reduction factor illustrate that the smaller probe, substrate height, and higher  $\lambda_d$  have a

higher directivity and a smaller HPBW. Therefore, this verifies that the electrical length is important and specific for a given taper for sharper beam shaping.

Table 4. Antenna model with an 8.0% taper compared to an electrically modified model and the original model with matching  $h/\lambda_d$  heights.

% Change from each ring to ring interface	Ring	1	2	3	4	5	6	7	8	9	10	11	12	13	14	15	16	17	18	19	20	21	22
10%	$\epsilon_r$	10.0	9.0	8.1	7.3	6.6	5.9	5.3	4.8	4.3	3.9	3.5	3.1	2.8	2.5	2.3	2.1	1.9	1.7	1.5	1.4	1.2	1.1
Substrate Height 14.8 mm $h/\lambda_d=0.10$																							
8%	$\epsilon_r$	5.8	5.3	4.9	4.5	4.2	3.8	3.5	3.2	3.0	2.7	2.5	2.3	2.1	2.0	1.8	1.7	1.5	1.4	1.3	1.2	1.1	1.0
Substrate Height 14.8 mm $h/\lambda_d=0.13$																							
8%	$\epsilon_r$	5.8	5	5	5	4	4	4	3	3	3	3	2	2	2	2	2	2	1	1	1	1	1
Substrate Height 15.5 mm $h/\lambda_d=0.10$																							

Another investigation will be used to see what happens if a constant base dielectric ring with a gradually decreasing taper is used. This decrease in taper will also slightly increase the end ring dielectric value from the previously ideal value of one. The last three plots compared the base dielectric varying from  $\epsilon_r = 10.0$  to 2.4. In the next set of simulations

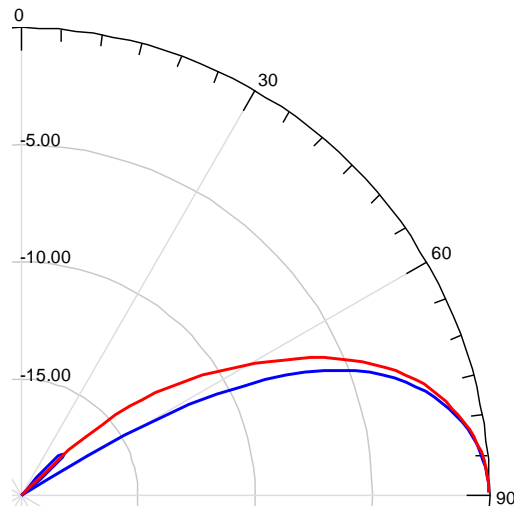


Figure 23. Normalized polar plot (in dB) of far-field pattern ( $E_{el}$  polarization) for an electrically modified 8.0% antenna (red) vs. a non-altered 8.0% antenna (blue).

the base dielectric will be kept the same at 4.6, and the tapers will gradually decrease which will naturally result in a higher outer ring dielectric constant as seen in Table 5.

The 6% change antenna had the highest half-power beamwidth of  $17.0^\circ$  as seen in Figure 24. The next three antennas have the outer ring to air dielectric difference steadily increase with a lower gradual taper. The next three antennas have half-power beamwidths of  $15.0^\circ$ ,  $14.0^\circ$ , and  $13.0^\circ$  respectively for 5.0%, 4.0%, and 3.0% tapered antennas. The lower tapered antennas with increased end ring dielectrics caused an increase in sidelobe level which grows from -13.1dB to -8.4 dB. This clearly shows that a relationship between the beamwidth and sidelobe levels exists. This relationship can be modified through a more gradual taper and a higher end ring dielectric constant interface with air, which can be greater than one.

Table 5. Dielectric distribution with fixed base dielectrics and varying percent reductions with increasing outer ring dielectrics.

% Change from each ring to ring interface	Ring	1	2	3	4	5	6	7	8	9	10	11	12	13	14	15	16	17	18	19	20	21	22
6%	$\epsilon_r$	4.6	4.32	4.06	3.82	3.59	3.38	3.17	2.98	2.80	2.64	2.48	2.33	2.19	2.06	1.93	1.82	1.71	1.61	1.51	1.42	1.33	1.25
5%		4.6	4.37	4.15	3.94	3.75	3.56	3.38	3.21	3.05	2.90	2.75	2.62	2.49	2.36	2.24	2.13	2.02	1.92	1.83	1.74	1.65	1.57
4%		4.6	4.42	4.24	4.07	3.91	3.75	3.60	3.46	3.32	3.19	3.06	2.94	2.82	2.71	2.60	2.49	2.39	2.30	2.21	2.12	2.03	1.95
3%		4.6	4.46	4.33	4.20	4.07	3.95	3.83	3.72	3.61	3.50	3.39	3.29	3.19	3.10	3.00	2.91	2.83	2.74	2.66	2.58	2.50	2.43

Based upon the above concepts a very low permittivity taper can be seen in Table 6. Here the base  $\epsilon_r = 1.47$  and is tapered at 1% with 22 rings. This design has one of the highest directivities obtained, with a HPBW of  $11.5^\circ$ . However, the dielectric base is getting close to  $\epsilon_r \approx 1$ . So this model's results obtained from the "wedge" were compared to the full scale model, seen in Figure 25.

Surprisingly the HPBW is exactly the same and does not suffer from the low

dielectric effects previously identified by the single dipole radiation pattern for the “wedge” model. The side lobe levels are however slightly increased by 0.5 dB and 5 dB for the first and second side lobes, respectively. The higher error in the second side lobe is expected as the lobe falls into the masking region of the “wedge” model. This error becomes more prevalent and will be explained in more detail in the following section. This slight increase in the side lobe levels is however, easily corrected if the height of the substrate is slightly lowered from 95 mm to 92 mm, as seen in Figure 26.

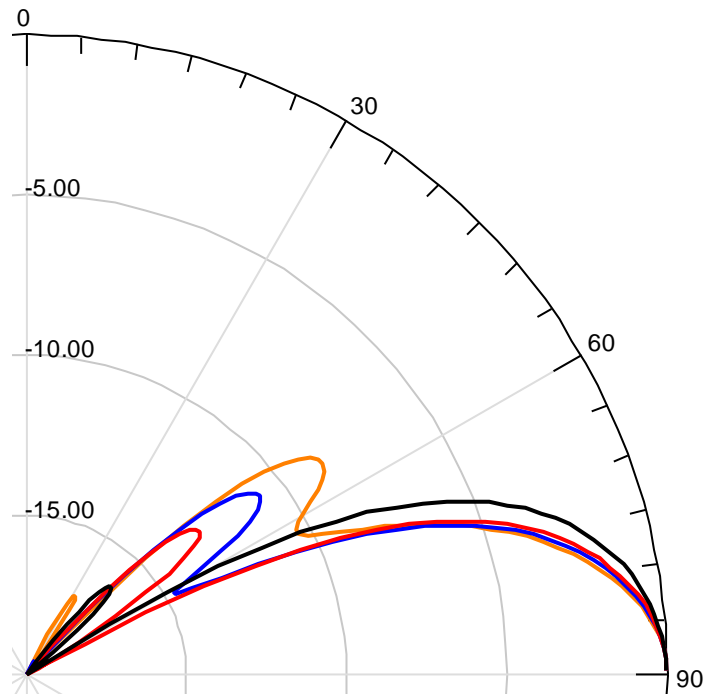


Figure 24. Normalized polar plot (in dB) of the far-field pattern ( $E_{el}$  polarization) for a tapered structure with 6.0% (black), 5.0% (red), 4.0% (blue) and 3.0% (orange) reductions.

Table 6. Dielectric distribution for 1% tapered DSWA.

% Change from each ring to ring interface	Ring	1	2	3	4	5	6	7	8	9	10	11	12	13	14	15	16	17	18	19	20	21	22
1%	$\epsilon_r$	1.47	1.46	1.44	1.43	1.41	1.40	1.38	1.37	1.36	1.34	1.33	1.32	1.30	1.29	1.28	1.26	1.25	1.24	1.23	1.21	1.20	1.19

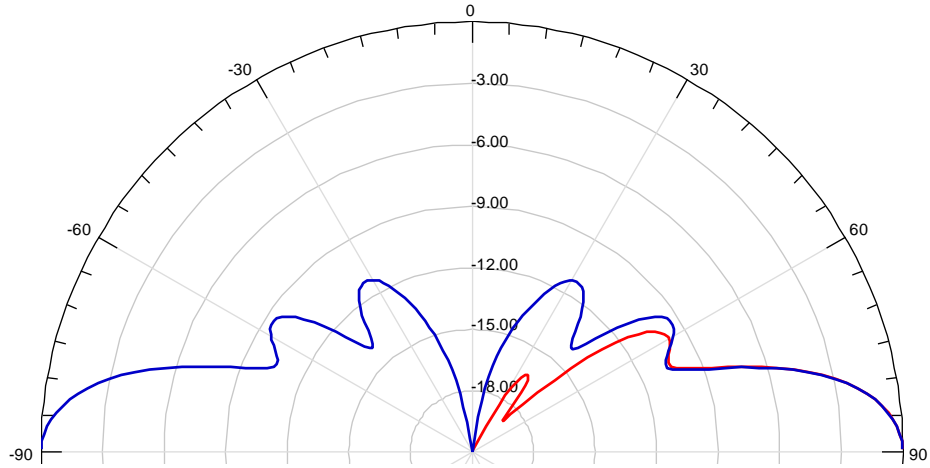


Figure 25. Normalized polar plot (in dB) of the far-field pattern ( $E_{el}$  polarization) for a 1% tapered structure with a base  $\epsilon_r = 1.47$ , simulated using the  $10^\circ$  “wedge” model (red) vs. the full scale model (blue).

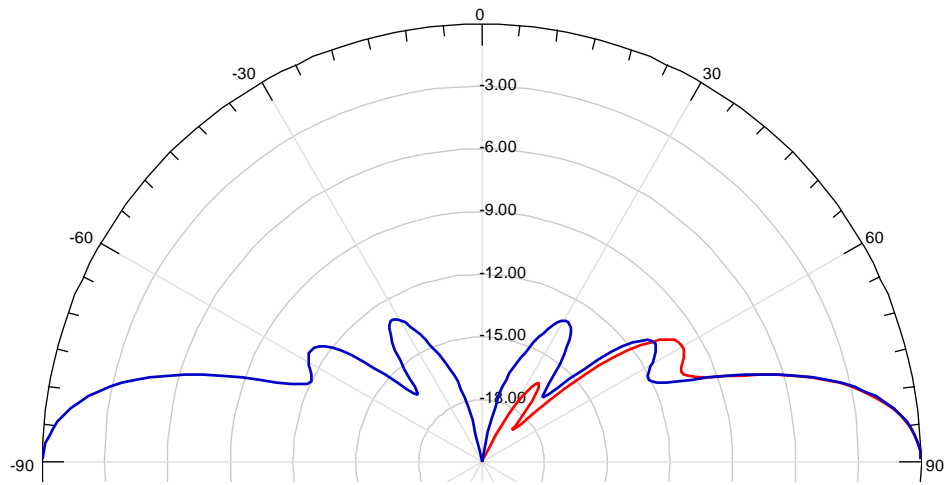


Figure 26. Normalized polar plot (in dB) of the far-field pattern ( $E_{el}$  polarization) for a 1% tapered structure with a base  $\epsilon_r = 1.47$ , using the  $10^\circ$  “wedge” model (red) vs. the full scale model with altered height (blue).

## 2. Individually Optimized Taper

Another approach that was considered was to manually optimize each ring separately from the other rings. The 10 ring model with  $1 < \epsilon_r < 10.0$  was used for this analysis. The inner ring was then set through an optimization scheme in HFSS that would analyze the E-field strength at endfire at various values of  $\epsilon_r$ . Permittivity values were typically chosen from 1-12 with a step increment around 0.5. Although the polar plots could not be directly viewed, the values of the directivity and normalized E-field strength at endfire for every angle  $\theta$  could be analyzed. The optimum  $\epsilon_r$  that was kept provided the highest directivity while keeping a primarily dominant surface wave with low side lobes. This optimum  $\epsilon_r$  was then plugged into the model, and the next ring was analyzed with the same method. Three iterations were used to fine tune the model as the values would eventually converge on a single value or a very close range. Table 7 shows an original model compared to an optimized model. Higher directivities were obtained with very narrow beamwidth when compared to the original “wedge” model as seen in Figure 27. However, when the optimized taper was compared to a full scale model as seen in Figure 28, there appeared very large side lobes near  $\theta = 6^\circ$  and  $18^\circ$ . This flaw in the “wedge” model was not realized until the end of this research study. Therefore, multiple simulations show there is a gradually increasing “masking” region between  $0 < \theta < 30^\circ$ . Fortunately, most DSWA designs do not suffer from these large sidelobes. It is expected that the higher end ring dielectric is producing a standing wave. Higher reflections would also occur from this taper, which produce the very strong side lobes. This is consistent with dielectric rod theory that a tapering scheme needs to be very gradual in order to obtain good beam sharpening. This approach could easily be redone

on a full scale model accurately with assuredly better results, but it would take a significantly longer time, which could not be accommodated here.

A similar approach was also used for individual ring lengths. These results were inconclusive due to the fact that as the individual rings gradually increased, so did the directivity, which made it more complex to analyze since the larger a structure is, the more directive it will naturally become.

Table 7. Optimization results for individual ring permittivity vs. a linear taper model.

	Ring	1	2	3	4	5	6	7	8	9	10
Linear Taper	$\epsilon_r$	10.0	9.0	8.0	7.0	6.0	5.0	4.0	3.0	2.0	1.0
Optimized Taper	$\epsilon_r$	10.0	10.0	9.0	6.7	5.0	4.0	4.0	3.8	1.0	6.0

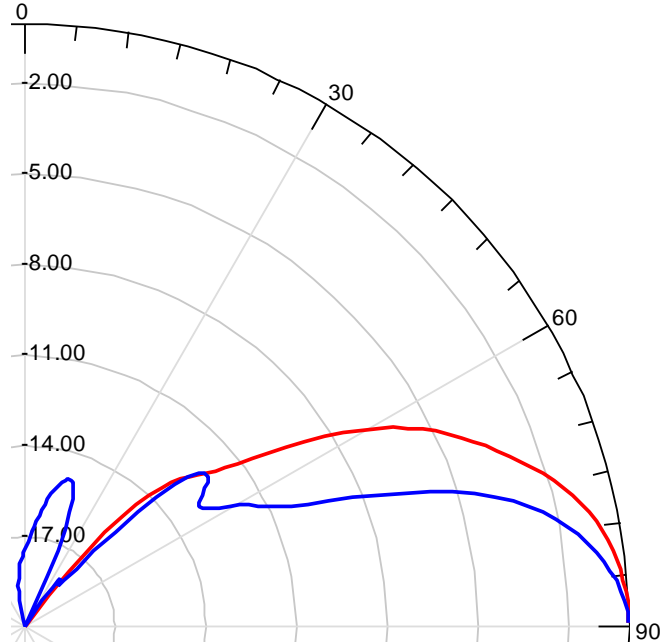


Figure 27. Normalized polar plot (in dB) of the far-field pattern ( $E_{el}$  polarization) for a linear taper (red) vs. an optimized taper (blue) using the “wedge” model.

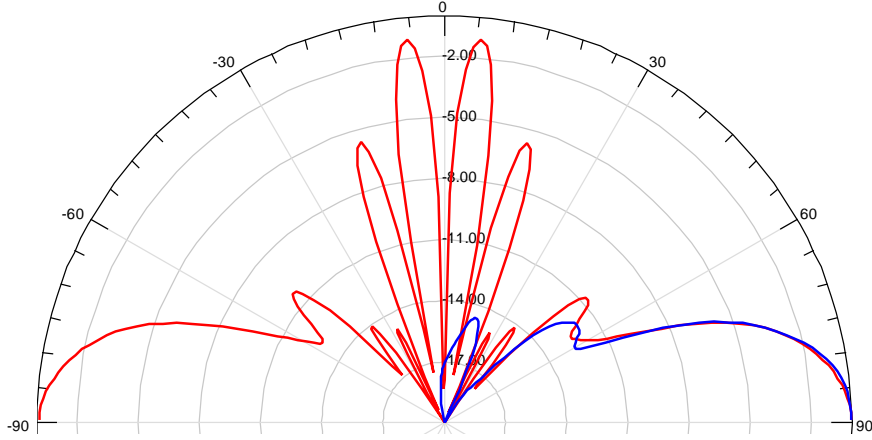


Figure 28. Normalized polar plot (in dB) of the far-field pattern ( $E_{el}$  polarization) of the optimized taper using the full scale model (red) vs. the “wedge” model (blue).

### 3. Equation-Based Dielectric Distribution

Fourteen equations were analyzed as seen in Appendix A to achieve a maximally directive patterned. The first equations to be analyzed produced a linear, cubic, quadratic, and 4<sup>th</sup> order polynomial dielectric tapers on a DSWA with base  $\epsilon_r = 3.7$  with an optimized substrate height of 15.6 mm. The linear taper had a much narrower HPBW and higher directivity as seen in Figure 29. The higher order polynomial equations have higher dielectric percentage change early within the distribution which causes the radiation pattern to flare significantly.

Other more complex equations were analyzed such as variations on the Gaussian on a Pedestal (GP) distribution

$$\epsilon_r(\rho) = \left( \frac{\epsilon_r(0) - 1}{1 - e^{-1}} \right) e^{-(\rho/R)^2} + \left[ 1 - \left( \frac{\epsilon_r(0) - 1}{1 - e^{-1}} \right) e^{-1} \right]. \quad (1)$$

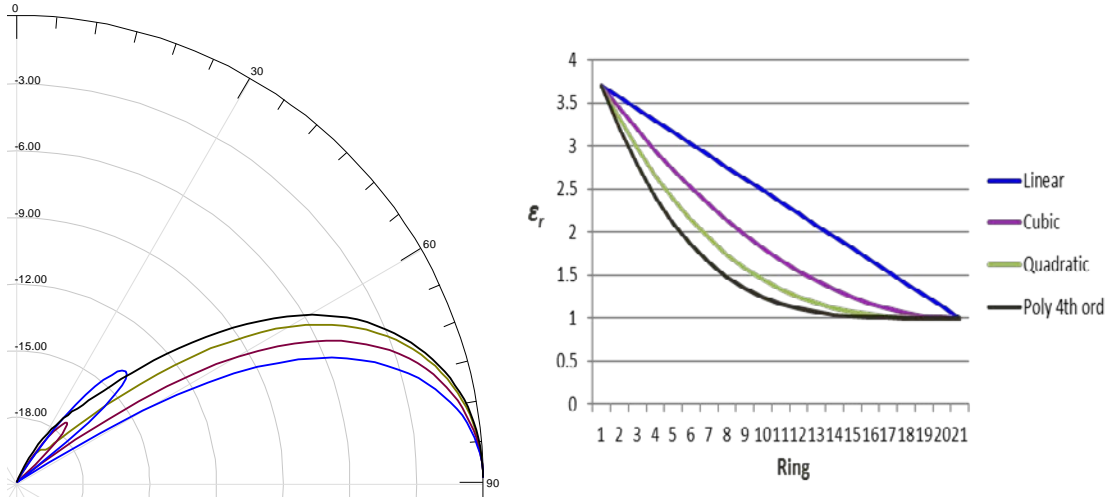


Figure 29. Normalized polar plot (in dB) of the far-field pattern ( $E_\theta$  polarization) for the linear taper (blue), cubic taper (purple), quadratic taper (green) and polynomial 4<sup>th</sup> order (black) (left) and  $\epsilon_r$  vs. ring distribution (right).

This equation takes on higher-order forms with variations to  $\alpha$  and  $n$  in the following equation, which is referred to as Generalized Hyper-Gaussian on a Pedestal:

$$\epsilon_r(\rho) = \left( \frac{\epsilon_r(0) - 1}{1 - e^{-\alpha}} \right) e^{-\alpha(\rho/R)^n} + \left[ 1 - \left( \frac{\epsilon_r(0) - 1}{1 - e^{-\alpha}} \right) e^{-\alpha} \right]. \quad (2)$$

Various trials of  $\alpha$  and  $n$  are used from 1-6 for each. The best results can be seen in Figure 30. When  $\alpha$  is kept low and  $n$  becomes increasingly smaller the HPBW converges to  $13.5^\circ$  with a directivity of 8.11 dB. However, the side lobe levels become larger than desired at -9.15 dB, so some additional manipulations may be needed in order to use this configuration.

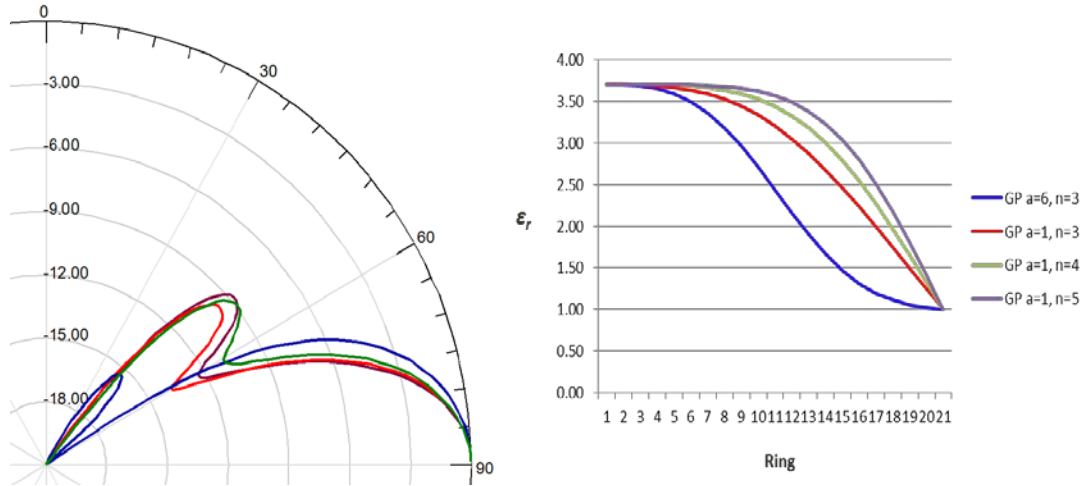


Figure 30. Normalized polar plot (in dB) of the far-field pattern ( $E_\theta$  polarization) GP ( $\alpha = 6, n=3$ ) (blue), GP ( $\alpha = 1, n = 3$ ) (red), GP ( $\alpha = 1, n = 4$ ) (green) and ( $\alpha = 1, n = 5$ ) (purple) (left).  $\epsilon_r$  vs. ring distribution (right).

Other equations were analyzed and a summary of all “best breed” models can be seen in Table 8. The Generalized Hyper Gaussian on a Pedestal equation had some of the most competitive directivities and beamwidth characteristics compared to other equation distributions. However, the lower more gradual dielectric linear tapers still gave the highest achieved results.

#### 4. Probe Height

Various probe heights were analyzed on two separate models. The first model used a base  $\epsilon_r = 1.47$  with a 1% taper. This model had one of the highest directivities at 8.43 dB with an initial probe height of 75 mm with a ring height of 92 mm. HFSS optimization was used to analyze the probe height from 45 mm to 86 mm. Figure 31 shows that the directivity of the DSWA can be increased to 9.48 dB by lowering the probe height to 65 mm. Figure 32 shows that not only has the directivity increased but

Table 8. Dielectric distribution summary table with comparison of beamwidth, side lobe level, and directivity.

Taper Scheme or Equation	Beamwidth [deg]	Side lobe level [dB]	Directivity [dB]
Exponential (6% Taper w/base $\epsilon_r$ 4.6) h = 14.8 mm	17.0	-13.1	8.19
Exponential (5% Taper w/base $\epsilon_r$ 4.6) h = 14.8 mm	15.0	-12.9	8.37
Exponential (4% Taper w/base $\epsilon_r$ 4.6) h = 14.8 mm	14.0	-10.9	8.39
Exponential (3% Taper w/base $\epsilon_r$ 4.6) h = 14.8 mm	13.0	-8.4	8.20
Exponential (2% w/ base $\epsilon_r$ 3.7) optimized h =15.6 mm	13.5	-10.7	8.41
Exponential (1% Taper w/base $\epsilon_r$ 1.47) optimized h = 92 mm	11.5	-10.5	8.43
Linear	16.5	-13.0	7.90
Cubic	19.5	-17.6	7.00
Quadratic	22.5	-19.2	6.45
Poly 4th Order	24.5	-21.1	6.00
Generalized Hyper Gaussian on a Pedestal (GHGP) a=1, n=2	15.5	-11.4	8.00
GHGP a=2, n=2	16.0	-13.2	7.80
GHGP a=3, n=2	17.0	-15.0	7.60
GHGP a=4, n=2	18.0	-16.7	7.40
GHGP a=5, n=2	19.0	-17.5	7.20
GHGP a=6, n=2	19.5	-19.0	7.10
GHGP a=1, n=3	14.5	-10.9	8.17
GHGP a=6, n=3	17.5	-15.3	7.72
GHGP a=1, n=4	13.5	-9.2	8.15
GHGP a=1, n=5	13.5	-9.1	8.11
Cosine on Pedestal	16.5	-15.4	7.76
Tanh with breakpoint in the middle	17.5	-15.4	7.52
Tanh with arbitrary breakpoint a=6 b=4	14.5	-9.2	7.94
Tanh with quadratic argument	14.5	-10.5	7.95
Exp with quadratic	24.5	-21.0	5.87

\* all equation-based tapers used a base  $\epsilon_r$  of 3.7 with a ring height of 15.6 mm.

the sidelobe levels have been brought down from -10.46 dB to -15.40 dB. The HPBW, however, remains the same for all probe heights. A second DSWA model was simulated with  $\epsilon_r = 4.6$  with a 4% taper. This antenna was chosen due to its higher base dielectric

constant. The height of this structure is 14.8 mm. The probe was varied from 5 mm to 17 mm. Figure 33 shows the directivity oscillating within a fairly small range of 8.49 dB to 8.54 dB. Changes in values within such a small range are most likely noise from

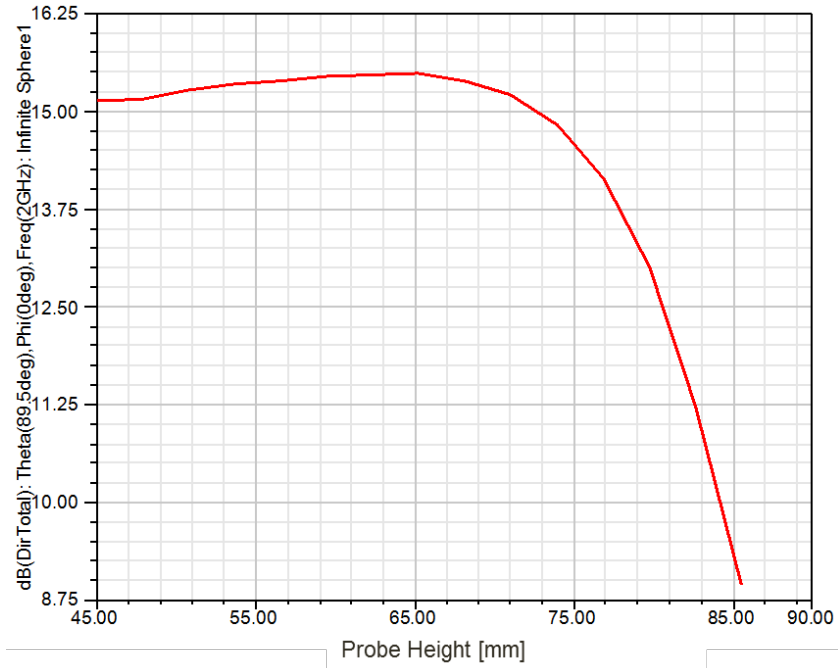


Figure 31. Directivity (in dB) for varying probe height at 2 GHz for a DSWA with  $\epsilon_r = 1.47$  with a 1% taper.

calculations within the model. Therefore, for higher dielectric constants, the probe height has little to no impact on the directivity. The total E-field in Figure 34 did increase from 13.4 dB to 22 dB (7.6 dB to 16.2 dB with the -5.79 correction factor). However, this is primarily due to a matching condition between the excitation wave port and the antenna.

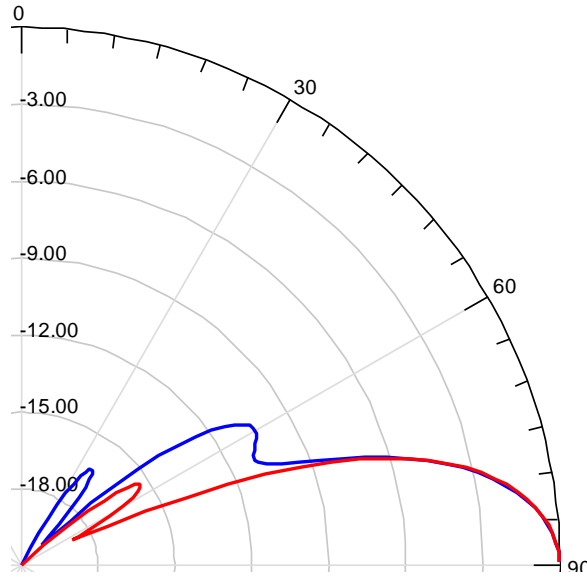


Figure 32. Normalized polar plot (in dB) of the far-field pattern ( $E_\theta$  polarization) for a DSWA with a base  $\epsilon_r = 1.47$  with a 1% taper and a probe height of 75mm (blue) vs. a probe height of 65 mm (red).

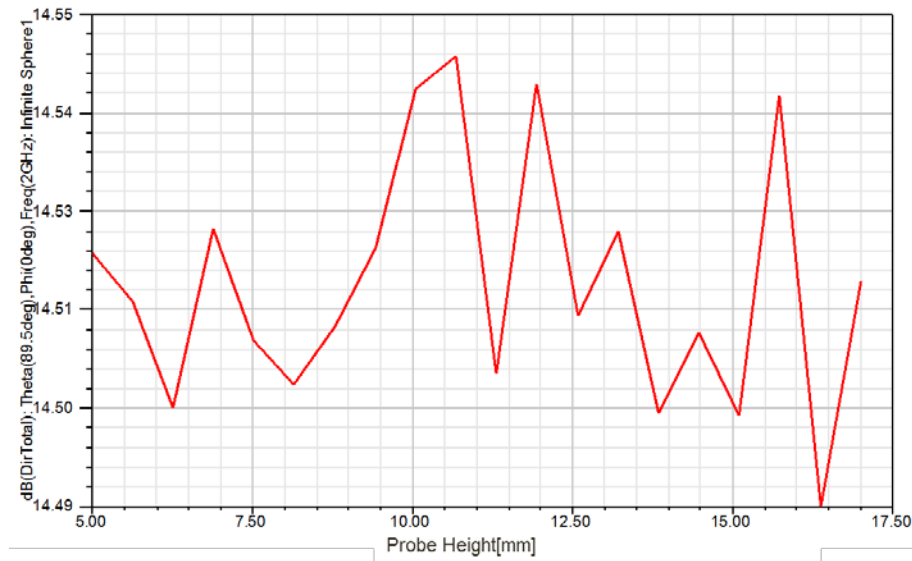


Figure 33. Directivity (in dB) vs. probe height for a DSWA with a base  $\epsilon_r = 4.6$  with a 4% taper.

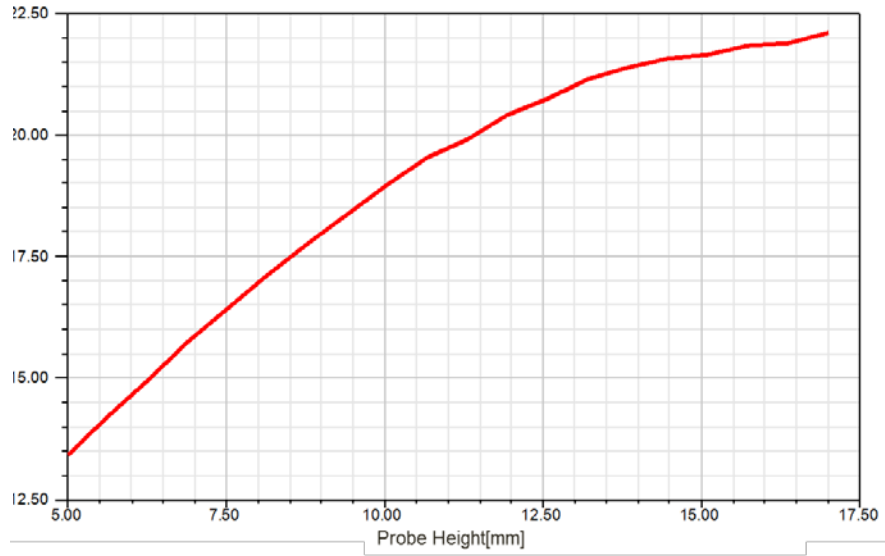


Figure 34. Total E-field (in dB) radiated at endfire for varying probe heights at 2 GHz, for a DSWA with a base  $\epsilon_r = 4.6$  and a 4% taper.

## Chapter 4

### 1. Analytical Pattern Formation

The following is based upon previous derivations and similar work [9]. An analytical approach was achieved through considering the array factor and by accounting for the  $TM_z$  polarization of the aperture field. An array factor for a circular ring with an arbitrary radius  $a$  is given by

$$AF(\theta) = \int_0^{2\pi} e^{jk_0(x' \sin \theta \cos \phi + y' \sin \theta \sin \phi)} a d\phi' . \quad (1)$$

For an arbitrary aperture distribution field distribution  $F(\rho)$  the array factor is

$$AF(\theta) = \int_0^{2\pi} \int_0^R F(\rho') e^{jk_0(x' \sin \theta \cos \phi + y' \sin \theta \sin \phi)} \rho' d\rho' d\phi' . \quad (2)$$

The exponential part is converted to cylindrical coordinates as

$$AF(\theta) = \int_0^{2\pi} \int_0^R F(\rho') e^{jk_0 \rho' (\sin \theta \cos \phi \cos \phi' + \sin \theta \sin \phi \sin \phi')} \rho' d\rho' d\phi' , \quad (3)$$

which can be further simplified to

$$AF(\theta) = \int_0^{2\pi} \int_0^R F(\rho') e^{jk_0 \rho' \sin \theta \cos(\phi - \phi')} \rho' d\rho' d\phi' . \quad (4)$$

The following Bessel function identity is helpful [8]:

$$AF(\theta) = \int_0^{2\pi} e^{jk_0 \rho' \sin \theta \cos(\phi - \phi')} d\phi' = 2\pi J_0(k_0 \rho' \sin \theta) . \quad (5)$$

Here  $J_0$  is the Bessel function of the first kind, order zero. Hence the array factor can be simplified to

$$AF(\theta) = 2\pi \int_0^R F(\rho') J_0(k_0 \rho' \sin \theta) \rho' d\rho' . \quad (6)$$

The DSWA aperture distribution can be approximated as the as that of a radial travelling wave with a known value of phase constant for any radius  $\rho$ . The phase constant  $\beta(\rho)$  can be approximated as that of an untapered DSWA at the radius  $\rho$ . The  $\beta(\rho)$  is found numerically from the TRE method that provides the wavenumber of the  $TM_0$  surface wave, using the permittivity and height of the ring at that radius  $\rho$ . The total phase of the aperture field at any radius  $\rho$  is then given by

$$\Phi(\rho') = -\int_0^{\rho'} \beta(\rho'') d\rho'' . \quad (7)$$

In order to account for both the amplitude and phase of the aperture field, the following aperture distribution is used:

$$F(\rho') = H_0^{(2)}(\Phi(\rho')). \quad (8)$$

The final array factor is then

$$AF(\theta) = 2\pi \int_0^R H_0^{(2)}(\Phi(\rho')) J_0(k_0 \rho' \sin \theta) \rho' d\rho'. \quad (9)$$

To account for the element pattern, the effects of the aperture polarization are used to include the element pattern of the  $\phi$ -directed magnetic surface current on the aperture.

This gives the result

$$E_\theta(\theta) = \int_0^{2\pi} \int_0^R F(\rho') e^{jk_0 \rho' \sin \theta \cos(\phi - \phi')} \cos \phi' \rho' d\rho' d\phi'. \quad (10)$$

The following Bessel function identity is then helpful [8]:

$$E_\theta(\theta) = \int_0^{2\pi} e^{jk_0 \rho' \sin \theta \cos(\phi - \phi')} \cos \phi' d\phi' = j2\pi J_1(k_0 \rho' \sin \theta). \quad (11)$$

This then provides the result

$$E_{\theta}(\theta) = 2\pi j \int_0^R H_0^{(2)}(\Phi(\rho')) J_1(k_0 \rho' \sin \theta) \rho' d\rho'. \quad (12)$$

## 2. Analytical Equation Validation

Both Matlab and Mathcad programs given in Appendix B were used to solve for the analytical form for  $E_{\theta}$ . The results showed a good correlation with work previously conducted on a 2-D leaky wave antennas for a  $20\lambda_0$  radius structure. This paper demonstrated a strong endfire condition when  $\beta(\rho)$  is set to the constant  $k_0$  as seen in Figure 35 [9]. Another confidence check was demonstrated for when  $\beta = k_0 \sin(45^\circ)$ , which showed a correct beam radiating at  $45^\circ$  as seen in Figure 36.

A tapering scheme for the linear model with  $\epsilon_r = (10, 9, 8, 7, 6, 5, 4, 3, 2, 1)$  from the inner ring to the outer ring was used. The program first provided the pattern for a non-tapered  $\beta = k_0$  which will be used as a basis for comparison with  $3.27\lambda_0$  radius which has been previously used in HFSS modeling as seen in Figure 37. Next, a tapered structure with  $\beta(\rho)$  is seen in Figure 38. The tapering scheme did not sharpen the beam as expected and actually produced higher side lobes near  $\theta = 5^\circ$  which are clearly not present in the HFSS model. So it is not a useful predictor of every tapering scheme and actually presented side lobe levels that are not typical. These lobes ranging near 0.5 on a linear scale (-6 dB) down from main lobe are much higher than any sidelobes that would be seen in HFSS for such a gradually tapered structure. So the model may not be a good quantitative predictor for beam shaping or directivity but it may provide qualitative insight into our model.

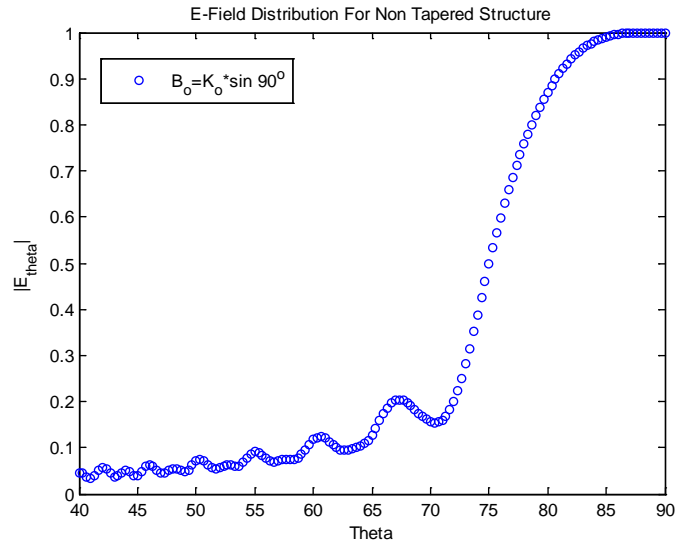


Figure 35. Matlab normalized plot (in dB) of the far-field pattern ( $E_{\theta}$  polarization)  $\beta = k_0$  for a  $20\lambda_0$  radius structure.

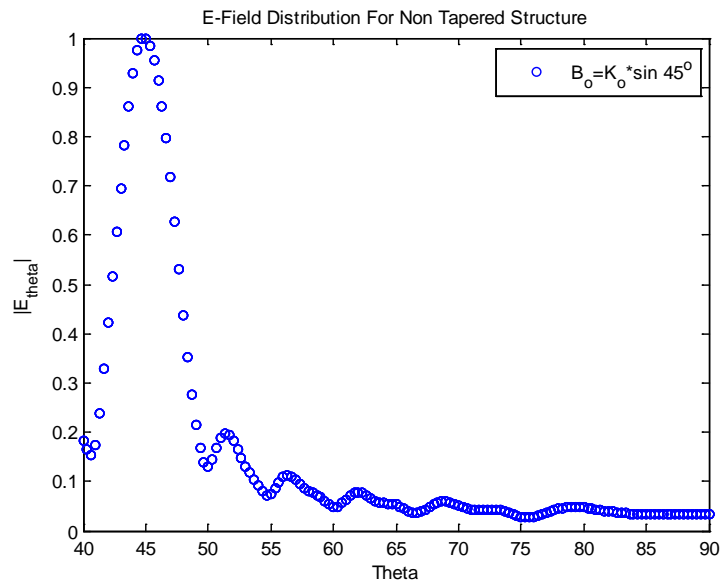


Figure 36. Matlab normalized plot (in dB) of the far-field pattern ( $E_{\theta}$  polarization) using  $\beta = k_0 \sin(45^{\circ})$  for a  $20\lambda_0$  radius structure.

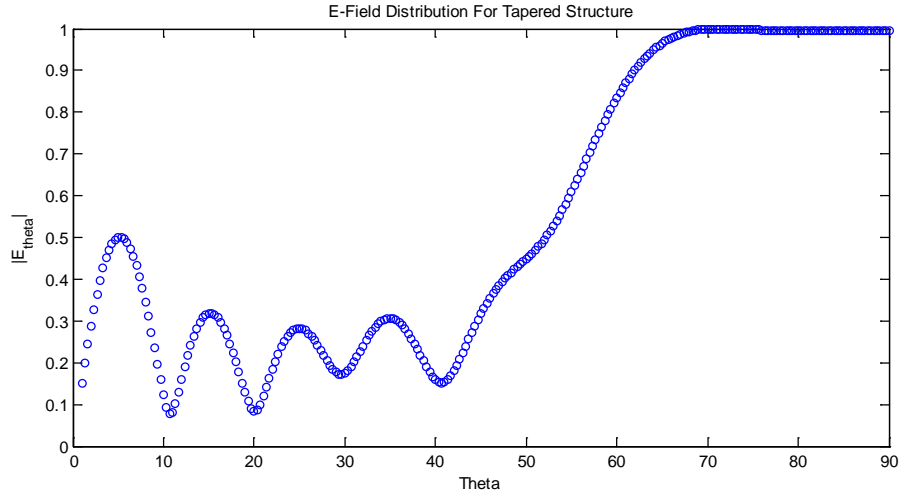


Figure 37. Matlab normalized plot (in dB) of the far-field pattern ( $E_\theta$  polarization) for a non-tapered structure with  $\beta = k_0$  for a  $3.27\lambda_0$  radius structure.

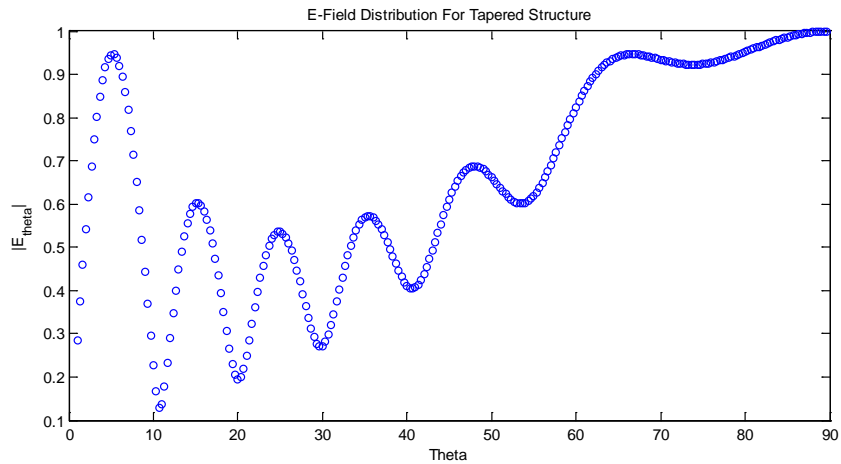


Figure 38. Matlab normalized plot (in dB) of the far-field pattern ( $E_\theta$  polarization) for a tapered  $3.27\lambda_0$  radius structure.

The model was then used to find what an ideal tapering scheme could produce. A simple linear taper in the wavenumber was used and modified iteratively to find the most directive beam. The highest normalized directivity result of 1.27 was obtained from a

linear wavenumber taper with a normalized  $\beta(\rho)$  varies from 1.267 to 1 as seen in Figure 39. Where the normalized  $\beta$  is equal to  $\beta/k_o$ . An exponential 0.1% taper in the wavenumber was also analyzed in a similar fashion which provided a higher normalized directivity of 3.08. The normalized  $\beta(\rho)$  varied from 1.267 to 1.134 as seen in Figure 40. The normalized directivity value was obtained from the inverse of the  $F$  function that is defined by

$$F = \int_0^{\frac{\pi}{2}} \frac{|E_\theta(\theta)|^2}{\left|E_\theta\left(\frac{\pi}{2}\right)\right|^2} \sin \theta d\theta. \quad (13)$$

The normalized average  $\beta$  ( $\beta_{\text{AVG}}$ ) values of the linear and exponential cases were 1.1335 and 1.1995, respectively.

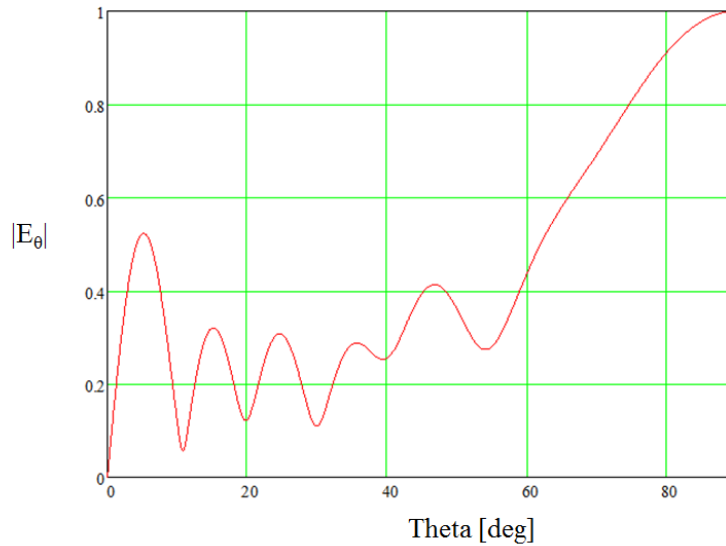


Figure 39. Mathcad normalized plot (in dB) of the far-field pattern ( $E_\theta$  polarization) for a linear tapered  $3.27\lambda_0$  radius structure with a maximum directivity.

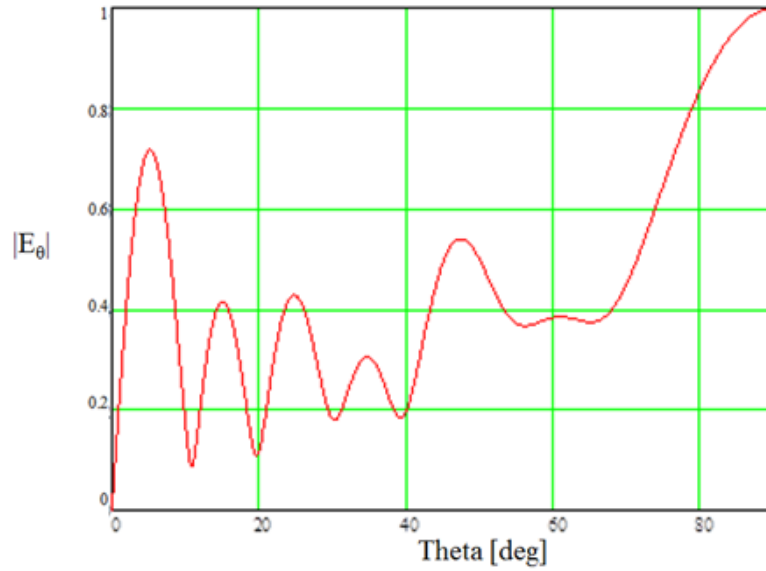


Figure 40. Mathcad normalized plot (in dB) of the far-field pattern ( $E_\theta$  polarization) for an exponential tapered  $3.27\lambda_0$  structure for maximum directivity.

The Hansen-Woodyard (HW) condition has been applied to leaky wave antenna theory [9,10]. The HW condition provides the optimum phase shift between the adjacent elements of a lossless antenna array in order to maximize the endfire directivity [11]. The optimum  $\beta_{HW}$  for a linear antenna array is expressed as

$$\beta = k_0 + \frac{2.94}{L}, \quad (14)$$

where  $k_0$  is the free-space wave number and  $L$  is the length of the array. The phase shift  $\beta_{HW}$  is typically just slightly larger than  $k_0$  and becomes smaller as the array increases in length. The numerator value of  $\tau = 2.94$  has been modified slightly for leaky wave applications in what has been referred to as a modified HW condition [9-10]. Applying this equation to our linear tapered structure with  $\tau = 2.75$  yields normalized  $\beta = 1.1335$  for a  $3.27\lambda_0$  structure. If a linear relationship existed for the  $\beta$  across the aperture then this

new modified HW condition could be potentially used for other DSWA designs. So the actual values found from HFSS are compared to the analytical model in Table 9.

Table 9. Analytical tapering analysis for highest directivity obtained for  $3.27\lambda_0$  structures, compared to  $\beta_{HW}$ .

<b>Analytical Model Tapering</b>	Inner $\beta$	Outer $\beta$	$\beta_{AVG}$	$\beta_{HW}$	$D_N$
Linear $\beta$	1.267	1.000	1.134	1.143	1.27
Exp 1% – 0.001% $\beta$	1.267	1.188	1.200	1.143	3.08

### 3. HFSS Modeling Based on the Hansen-Woodyard Condition

Based on the average optimized  $\beta$  a DSWA was modeled in HFSS with 22 rings with a 1% taper in the permittivity that has an average  $\epsilon_r = 1.403$ , which provided a desired an average normalized  $\beta$  of 1.1335 based on the analytical results. This antenna was then numerically optimized resulting in a substrate height of 121 mm and probe height of 71 mm which produced the highest directivity characteristics as seen in Figure 41. The average normalized  $\beta$  value shifted with the substrate height change from 1.1335 to 1.086. The directivity obtained was 9.8 dB with a beamwidth of  $11.5^\circ$ . Additional optimization was conducted with ring values with higher directivity values seen with a 0.01% taper with a  $\epsilon_r = 1.402$  base dielectric and a slightly higher average normalized  $\beta$  of 1.1017. Here the maximum directivity is 11.06 dB with a  $10^\circ$  beamwidth as seen in Figure 42. A table with values for both models is included in Appendix C.

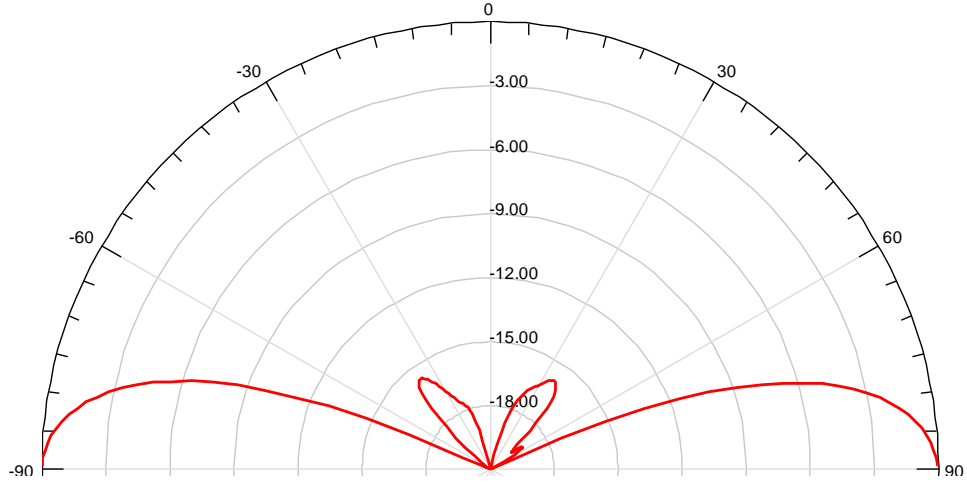


Figure 41. Polar plot (in dB) of the far-field pattern ( $E_\theta$  polarization) for a DSWA with a base  $\epsilon_r = 1.403$  and a 1% taper, with a height of 121 mm and a probe height of 71 mm.

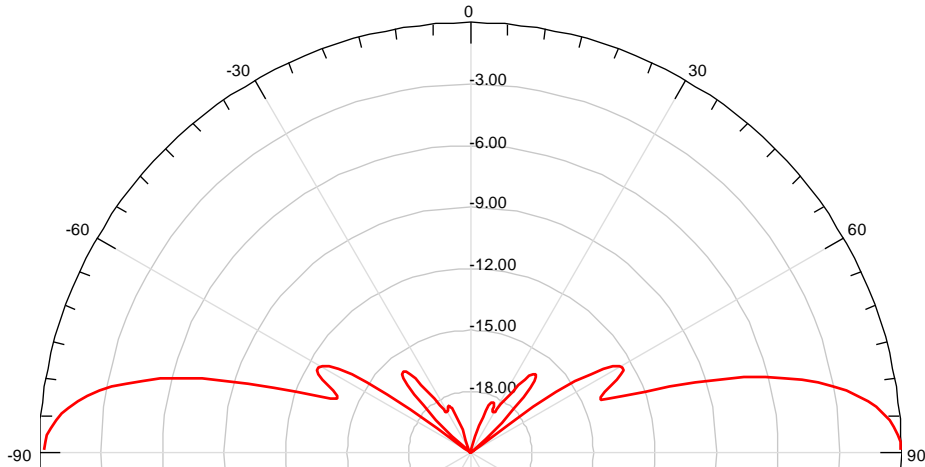


Figure 42. Polar plot (in dB) of the far-field pattern ( $E_\theta$  polarization) for a DSWA with a base  $\epsilon_r = 1.402$  and a 0.1% taper with a height 121 mm and a probe height of 71 mm.

Although the analytical model was not accurate for prediction of beamwidth or directivity, it did give us the ability to realize that a modified HW condition is present. This principle, although typically used for antenna arrays and leaky-wave antennas, can now be directly applied to our traveling surface-wave wave structure for an optimum

average normalized  $\beta$  value of 1.1017 which has given the highest results obtained with a 15% increase in directivity and a 13% decrease in beamwidth. Overall, the previous percent tapered antennas can be seen in Table 10 with the  $\beta_{\text{AVG}}$  values and their comparison to the  $\beta_{\text{HW}}$ . The  $\beta_{\text{AVG}}$  and  $\beta_{\text{HW}}$  are fairly close and typically offset by 0.03 to 0.09.

Next, a new set of linear  $\beta(\rho)$  designs were used to compare to the exponential  $\beta(\rho)$  designs. Initially, linearly tapered permittivity designs were not particularly useful when compared to the percent tapers (exponential tapers) in HFSS. However, combining linear permittivity tapers with  $\beta(\rho)$  closer to the HW condition provided higher directivities and a lower HPBW than previously seen on percent tapered DSWAs. It is important to note that a linear or percent tapered permittivity structure produces a linear or percent  $\beta(\rho)$ . Both linear and percent tapered DSWAs each have their optimum electrical size with a fixed  $\beta$  for optimum beam sharpening as seen in Figure 43. It is seen that if the electrical length is too small the highest directivity won't be achieved. And if the structure is too long then the main lobe pulls away from the surface. These effects become even stronger with linear tapered structures. Table 11 contains a range of optimized antennas with varying electrical lengths from  $0.46\lambda_0$  to  $12.5\lambda_0$ . These values are based solely on the "wedge" model results with a resulting estimated directivity due to time constraints. Therefore, values should be used only for initial design estimations. The  $\beta_{\text{AVG}}$  value for small structures does not match up well with the  $\beta_{\text{HW}}$ . However, as the structures become larger the values converge for the  $12.5\lambda_0$  DSWA designs to within a 3.9% difference from the predicted HW condition. There also exists a trending

decrease in the optimum initial  $\beta$  of the first dielectric ring as the structure becomes larger. This trending can be seen in Figure 44. This is very useful and provides an ideal starting value that varies only on the size of the structure so that the near optimum directivity and HPBW can be achieved.

Table 10. DSWA with varying percent permittivity tapers and a comparison to  $\beta_{AVG}$  and  $\beta_{HW}$ .

Exponential Tapers	Structure Length [ $\lambda_o$ ]	Beamwidth [deg]	Side lobe level [dB]	Directivity [dB]	Height [mm]	Probe Height [mm]	$\beta_{AVG}$	$\beta_{HW}$
6% Taper w/base $\epsilon_r$ 4.6	3.27	17.0	-13.10	8.19	14.8	14	1.0885	1.143
5% Taper w/base $\epsilon_r$ 4.6	3.27	15.0	-12.90	8.37	14.8	14	1.1030	1.143
4% Taper w/base $\epsilon_r$ 4.6	3.27	14.0	-10.90	8.39	14.8	14	1.1200	1.143
3% Taper w/base $\epsilon_r$ 3.7	3.27	14.0	-10.36	8.40	15.6	15	1.1261	1.143
2% Taper w/base $\epsilon_r$ 3.7	3.27	13.5	-10.67	8.41	15.6	15	1.1261	1.143
1% Taper w/base $\epsilon_r$ 1.47	3.27	11.5	-10.46	9.40	92.0	65	1.1126	1.143
1% Taper w/base $\epsilon_r$ 1.403	3.27	12.5	-17.05	9.60	121.0	71	1.0860	1.143
.1% Taper w/base $\epsilon_r$ 1.402	3.27	10.0	-13.12	11.06	121.0	71	1.0115	1.143
.1% Taper w/base $\epsilon_r$ 1.402	4.46	8.50	-11.17	12.19	137.5	71	1.0115	1.105
.1% Taper w/base $\epsilon_r$ 1.402	4.46	7.50	-10.68	14.37	150.0	71	1.0115	1.105
.1% Taper w/base $\epsilon_r$ 1.3	6.00	6.00	-13.01	16.21	150.0	71	1.0256	1.078

Table 11. DSWA with linear permittivity tapers and a comparison to  $\beta_{AVG}$  and  $\beta_{HW}$ .

Base Dielectric	Structure Length [ $\lambda_o$ ]	Beamwidth [deg]	Side lobe level [dB]	Directivity [dB]	Height [mm]	Probe Height [mm]	$\beta_{AVG}$	$\beta_{HW}$	Analytical Model $D_{norm}$
1.99	0.46	15.5	-10.33	2.81	125.0	71	1.061	2.142	1.17
1.90	0.93	14.3	-10.33	6.47	125.0	71	1.077	1.571	1.25
1.89	1.24	13.0	-11.97	9.15	125.0	71	1.070	1.430	1.21
1.85	1.86	10.5	-10.32	10.87	125.0	71	1.061	1.285	1.49
1.70	3.72	8.0	-10.01	11.04	132.0	71	1.067	1.143	2.00
1.50	7.43	5.5	-11.83	15.81	200.0	71	1.055	1.105	2.34
1.35	12.5	4.5	-12.35	19.11	240.0	71	1.036	1.040	3.41

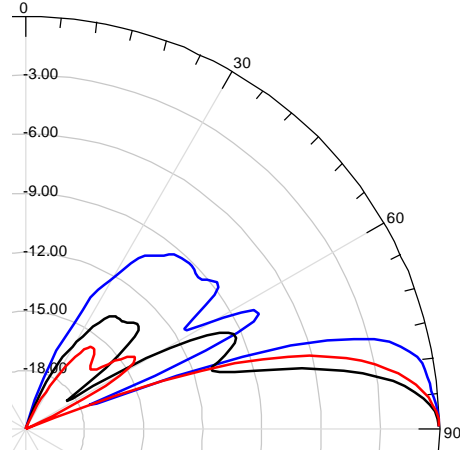


Figure 43. Polar plot (in dB) of the far-field pattern ( $E_\theta$  polarization) for a percent tapered DSWA of varied sizes  $3.27\lambda_0$  (red),  $4.5\lambda_0$  (black) and  $10\lambda_0$  (blue), for a fixed  $\beta$ .

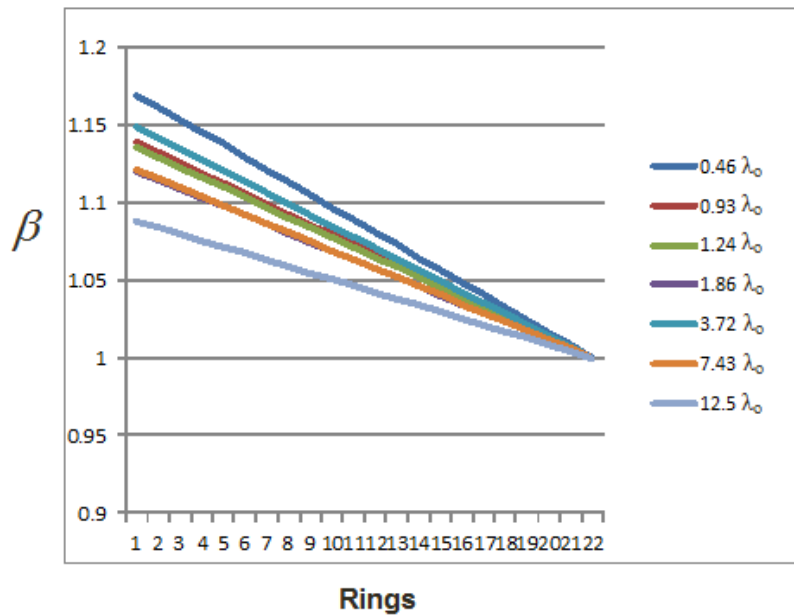


Figure 44.  $\beta$  vs. dielectric ring number for optimized  $0.46\lambda_0 - 12.5\lambda_0$  DSWA linear-tapered permittivity structures.

Based on the relationship of these linear tapered antennas an optimum design relationship can be seen in Figures 45-48. Here the optimal values (from HFSS) are plotted vs. electrical lengths. Ideally a designer can use this information such as initial  $\beta$ , height of substrate, beamwidth, and directivity to build a DSWA accordingly. It is

important to note that the substrate height values are based off of the dielectric properties of the antennas found in Table 11. However, alternate antennas could be built with higher dielectric properties which would require lower profile substrate heights to obtain the same initial  $\beta$  as found in Figure 45. The designer would simply have to use the TRE method to find the optimum height. For example an  $\epsilon_r = 10$  for a base dielectric would have a very low profile height of a few millimeters and it would require many more rings to minimize main lobe radiation degradation and reduce sidelobes to an acceptable level. In this case it is very likely a higher directivity and lower HPBW could be achieved. Due to time limitations those values could not be added into this case study. Lastly, full model verification with anticipated slightly modified design tables from the “wedge” model designs will be provided later in the future.

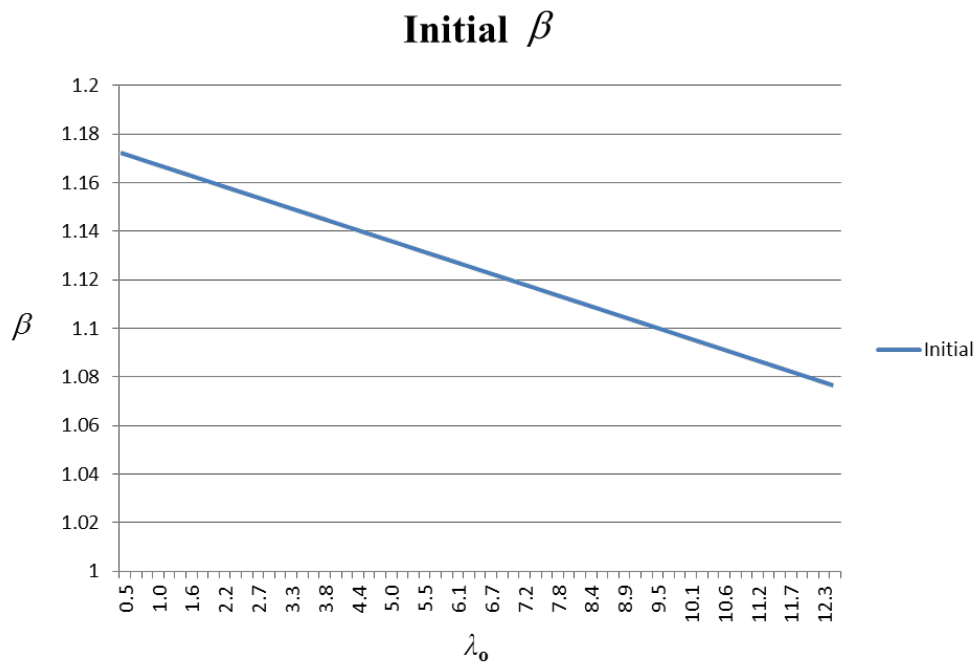


Figure 45. Initial  $\beta$  vs. radial size in  $\lambda_0$  for a structure with an optimized linear taper in the permittivity.

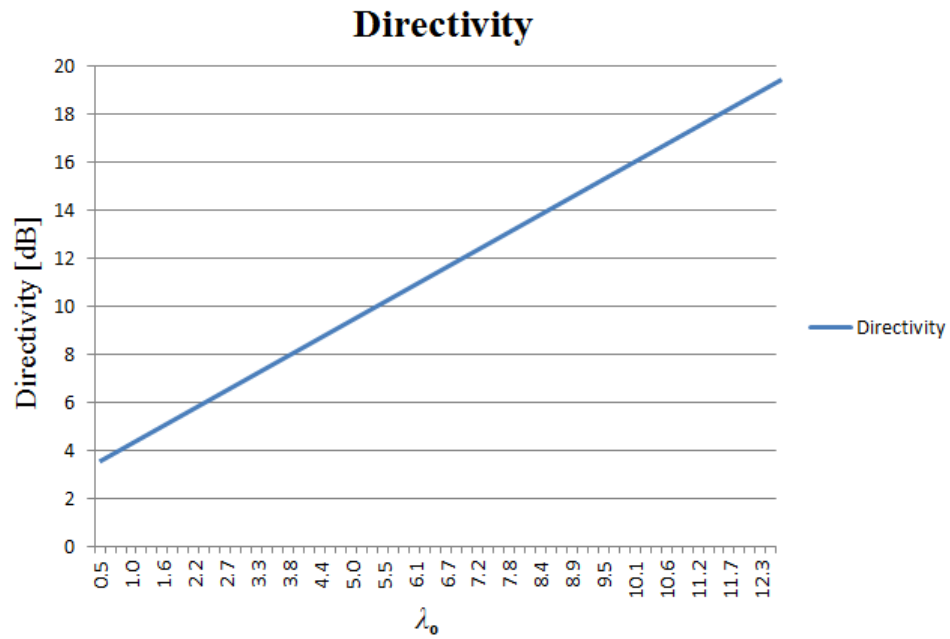


Figure 46. Directivity vs. radial size in  $\lambda_0$  for a structure with an optimized taper in the permittivity.

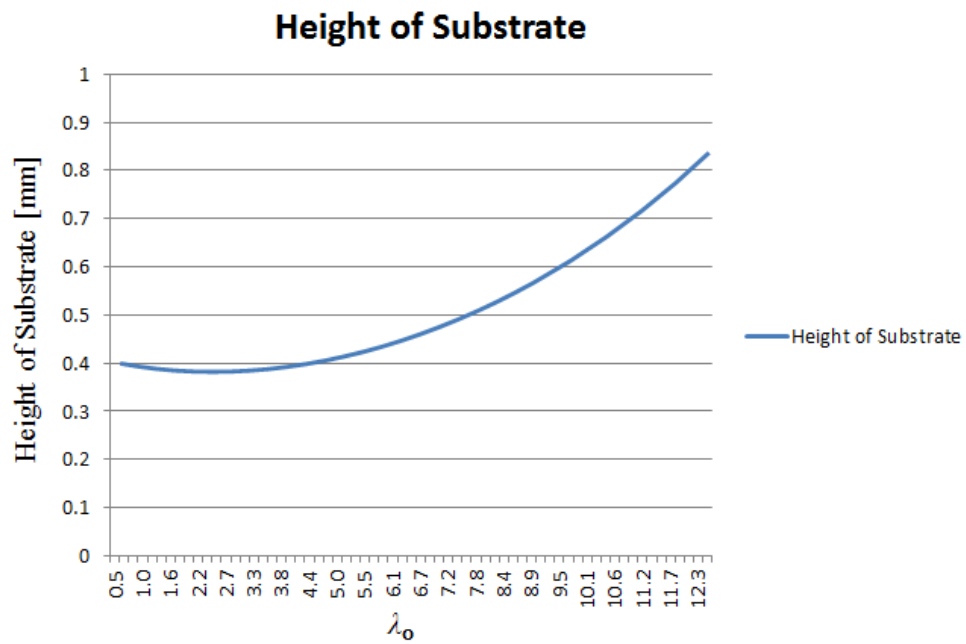


Figure 47. Height of substrate vs. radial size in  $\lambda_0$  for a structure with an optimized taper in the permittivity.

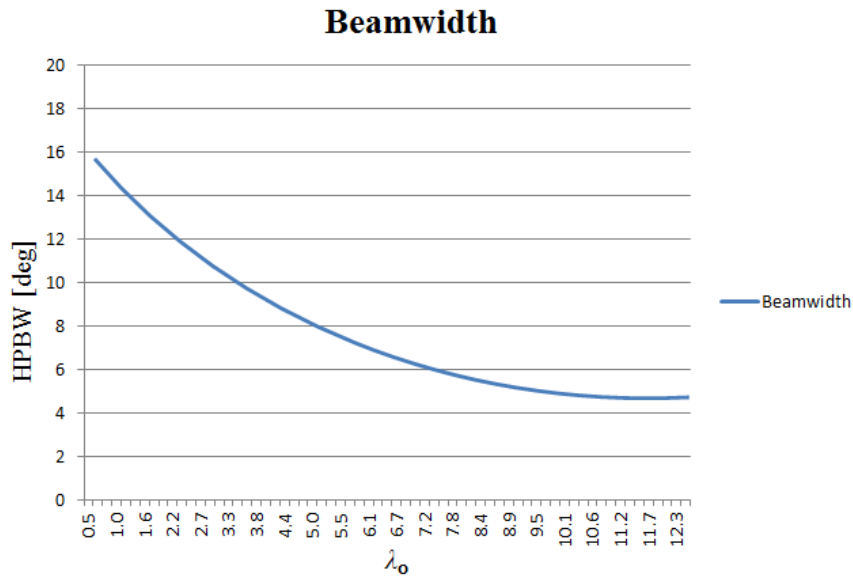


Figure 48. Beamwidth vs. radial size in  $\lambda_0$  for a structure with an optimized taper in the permittivity.

#### 4. Solver Comparison

Computer Simulation Technology (CST) Microwave Studios was successfully used to validate the results of HFSS for a single case study. A DSWA with a base  $\epsilon_r = 1.403$  and a 1% permittivity taper previously analyzed will be compared. HFSS uses a finite element method and CST Microwave Studios uses a finite integral technique with a perfectly matched boundary condition that is unique to the solver. Due to model limitations within CST a finite ground plane was used with an electrical length of  $6\lambda_0$  for both model computations. CST uses a full model comparison and HFSS uses a “wedge” model with radiation boundary above and below the ground plane. HFSS therefore has a faster converging solution than the CST model, which may give a reason for some model discrepancies. Overall the solvers provided very supportive evidence that this antenna

can produce directive beams very close to that predicted by the “wedge” model if an infinite or near infinite ground plane is present. A full model HFSS simulation was not attempted due to lack of memory required for such a solution. The results can be seen in Figure 49. Previously, a scale of -21 to 0 dB was typically used for most of the radiation plots for simplicity. However, this comparison will use a -50 to 0 dB scale. The CST radiation pattern has a main lobe at  $79^\circ$  with a beamwidth of  $11.6^\circ$ . The sidelobe levels range from -10.3 to -12 dB. There also exists a small artifact with a strong main lobe radiation at  $\theta = 0^\circ$  and  $\theta = 180^\circ$ . These radiation sidelobes are simply not possible or ever seen in HFSS models. A structure would have to be much longer to produce such a directive beam in this direction. This antenna excites a symmetric  $TM_0$  mode that naturally produces a null at  $\theta = 0^\circ$ . Therefore these strong lobes are likely due to some solver error or lower convergence value required for such a large structure. The HFSS produced radiation pattern has a main lobe at  $80^\circ$  with a beamwidth of  $9^\circ$ . The sidelobe levels range from -13 to -17 dB. There is also the anticipated sidelobe masking from  $\theta = 0^\circ$  to  $30^\circ$  and  $150^\circ$  to  $180^\circ$ . The infinite ground plane “wedge” model radiation pattern has a comparable beam width of  $10^\circ$  with lower sidelobe levels, which could be expected for an infinite ground plane. For the wedge models, there is only a weak radiation field in the negative  $\theta$  direction, while the full CT model shows a symmetric pattern, as expected. Simulated full patterns can be obtained from the wedge model patterns by reflecting the patterns across the  $z$  axis to make them symmetric.

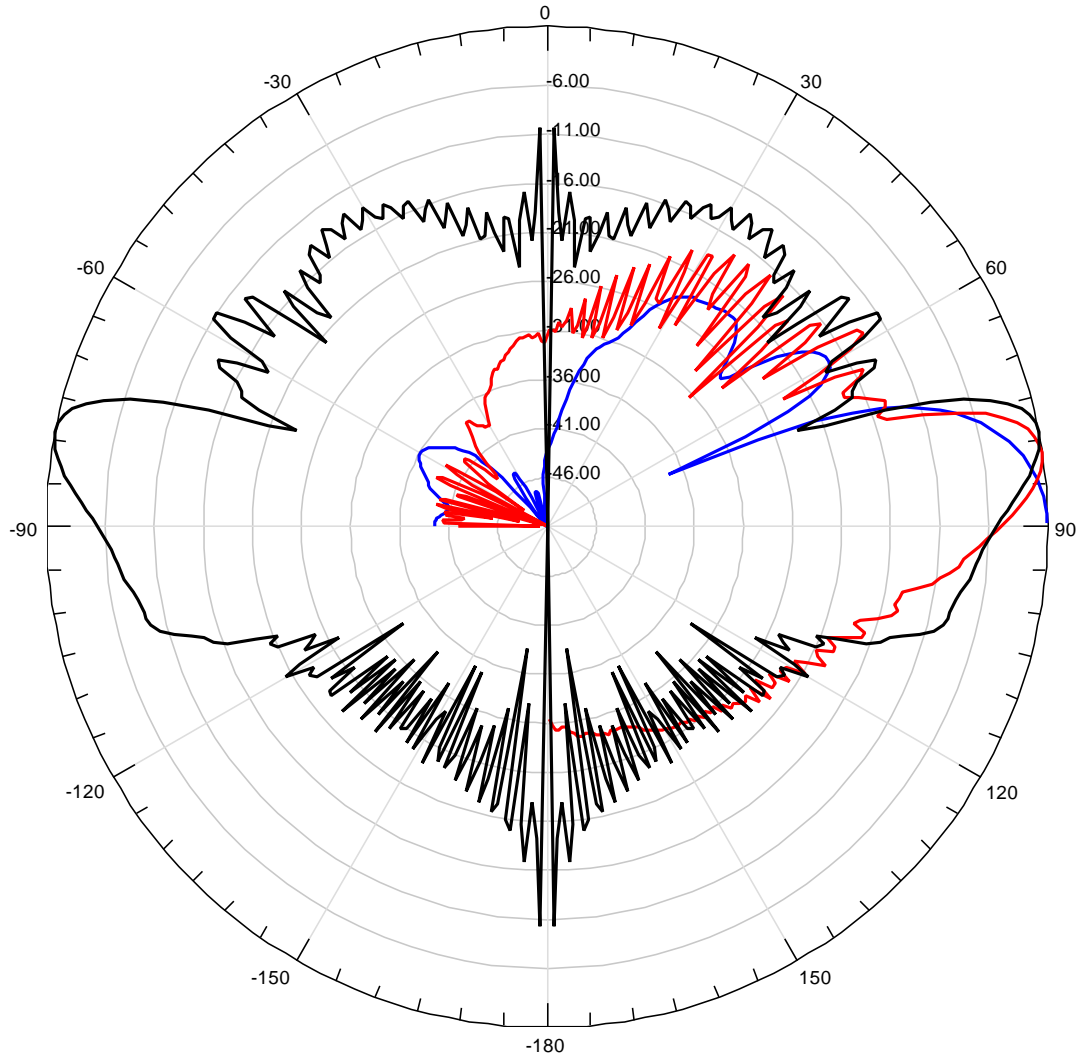


Figure 49. CST full model with a finite ground plane (black), HFSS “wedge” model with a finite ground plane (red), and an HFSS “wedge” model with an infinite ground plane (blue).

## Chapter 5

### Conclusion

A new type of dielectric surface wave antenna (DSWA) has been proposed, consisting of a tapered dielectric cylinder excited by a vertical probe at the center. Using  $0.46\lambda_0 - 12.5\lambda_0$  radii structures and a gradual radial taper in the relative permittivity and  $\beta$ , omnidirectional directive endfire beams can be produced. This provides antenna designers new options when omnidirectional directive beams at endfire are needed. Various optimization schemes were explored which include substrate height, taper schemes, probe height, and optimized  $\beta$  values. These variables were optimized to provide the strongest radiation at endfire. The wavenumber  $\beta$  of the  $TM_0$  surface wave is found from the TRE method, where the value is based on substrate height and a dielectric constant. As the size of the structures increases in the radial dimension, the average wavenumber on the structure  $\beta_{AVG}$  decreases, which results in consistently higher directivities and narrower beamwidths.

The HFSS model simulations were also supported by the analytical approach which provided qualitative insight into the Hansen-Woodyard (HW) condition. There exists a delicate relationship between how the analytical model can be used, specifically for smaller to very large structures. As the structures become very large, the theoretical optimized model will tend towards the HW condition. The HW condition states that the average  $\beta$  value for very large structures will converge to a value close to 1. This however, would eventually cause the antenna to give a radiation pattern that consists of mainly direct feed radiation, and narrow beam formation would not be possible. So the

analytical model is correct in a qualitative sense when it is used in the context that it provides an ideal  $\beta$  taper for a pure plane surface wave, which allows us to better understand the antenna. However the DSWA is a much more complex system than the analytical model, which doesn't account for the multiple reflections at each ring interface and direct feed radiation. The analytical model was also not an accurate predictor of beam or sidelobe formation. Therefore, HFSS was relied upon for optimization and pattern prediction over the analytical model.

A DSWA designer would ideally define a directivity, beamwidth, and frequency requirement and be able to design an antenna for a given radius to get the desired results. The beamwidth can be decreased to  $4.5^\circ$  for a  $12.5\lambda_0$  structure. The  $3.27\lambda_0$  radius structure has been analyzed extensively and better results cannot be reasonably obtained based on the discussed design specifications. These design specifications can be used to create other optimized antennas of varied electrical lengths now that an initial estimated relationship has been established. Simulations were limited to the size of the structure and the number of rings provided for tapering which ranged from 10-25 rings. One important consideration for these antennas is to add additional rings if a higher directivity and lower sidelobes is required, since more rings produce a continuously smoother radiation main lobe. Sidelobes will also be reduced to a much greater extent.

These designs naturally have some realistic fabrication challenges. Manufacturing inconsistencies in dielectric constants are typical and values are not generally homogenous or accurate enough within a reasonable cost for most of the higher directivity designs. So a material with consistent and low variable dielectric constant is required at a higher cost. Combining multiple rings of varied dielectric constants and

obtaining a good seal between rings will also prove difficult. Another option available to DSWA designers is to drill holes in a higher dielectric duroid board. Drilling holes would lower the dielectric properties of a specific region so that the surface wave would ideally see an increasingly smaller average dielectric constant produced by the air holes as it encounters areas (rings) with a higher perforation. Another approach could be to mill rings into the substrate. This milling would produce effective air gaps. These gaps, if made thin enough compared to the wavelength, would lower the effective permittivity of the ring region while keeping the ring permittivity nearly homogeneous on the scale of the ring.

## References

- [1] S. A. Long, M. W. McAllister and L. C. Shen, "The resonant cylindrical dielectric cavity antenna," *IEEE Trans. Antennas and Propagation*, vol. 31, pp. 406 – 412, May 1983.
- [2] K. M. Luk, and K. W. Leung (Eds.), Dielectric Resonator Antennas, Research Studies Press, 2002.
- [3] A. P. Huynh, D. R. Jackson and S. A. Long, "Reduced lateral wave cylindrical dielectric resonator antenna," *2009 AP-S International Symp.*, pp. 1 – 4, July 2009.
- [4] F. J. Zucker, "Surface-wave antennas," in *Antenna Engineering*, R.C. Johnson, Ed., 3rd ed. New York: McGraw-Hill, 1993, ch. 12.
- [5] D. G. Kiely, "Dielectric aerials", Methuen Monograph, London 1953.
- [6] J. R. James, "Engineering approach to the design of tapered dielectric-rod and horn antennas," *The Radio and Electronic Engineer*, vol. 42, pp. 251-259, Jun. 1972.
- [7] S. K. Mustafa and S. Yasir, "Design, development and testing of dielectric tapered rod feed for parabolic reflector antenna as an alternate to feed horns," *2010 IBCAST International Conference*, pp. 369-371, Jan 2013.
- [8] C. A. Balanis, *Antenna Theory, Analysis and Design*, 3<sup>rd</sup> ed., Hoboken, NJ: Wiley, 2005.
- [9] C. Zhang, D. R. Jackson, and S. A. Long, "Hansen-Woodyard condition for leaky-wave antennas," *IEEE Trans. Antennas and Propagation* (in press).
- [10] E. M. O'Connor, D. R. Jackson, and S. A. Long, "Extension of the Hansen-Woodyard condition for endfire leaky-wave antennas," *IEEE Antennas and Wireless*

- Propagation Letters*, vol. 9, pp. 1201-1204, Nov. 2010.
- [11] W. W. Hansen and J. R. Woodyard, "A new principle in directional antenna design," *Proc. of the Institute of Radio Engineers*, vol. 26, no. 3, pp. 333-345, March 1938.
- [12] A. Al-Zoubi, A. F. Yang and A. Kishk, "A low-profile dual-band surface wave antenna with a monopole-like pattern," *IEEE Trans. Antennas and Propagation*, vol. 55, pp. 404-412, Dec. 2007.
- [13] L. B. Felsen, "Radiation from a tapered surface wave antenna," *IRE Trans. Antennas and Propagation.*, vol. AP-8, pp. 577-586, Nov. 1960.

## Appendix

### A. Taper Distribution Equations

1) Linear

$$\varepsilon_r(\rho) = \varepsilon_r(0) - \left( \frac{\varepsilon_r(0) - 1}{R} \right) \rho$$

2) Quadratic (flat at  $\rho = R$ )

$$\varepsilon_r(\rho) = \left( \frac{\varepsilon_r(0) - 1}{R^2} \right) (R - \rho)^2 + 1$$

3) Cubic (flat at  $\rho = R$ )

$$\varepsilon_r(\rho) = \left( \frac{\varepsilon_r(0) - 1}{R^3} \right) (R - \rho)^3 + 1$$

4) Polynomial ( $n$  is arbitrary)

$$\varepsilon_r(\rho) = \left( \frac{\varepsilon_r(0) - 1}{R^n} \right) (R - \rho)^n + 1$$

5) Exponential on a Pedestal

$$\varepsilon_r(\rho) = \left( \frac{\varepsilon_r(0) - 1}{1 - e^{-1}} \right) e^{-(\rho/R)} + \left[ 1 - \left( \frac{\varepsilon_r(0) - 1}{1 - e^{-1}} \right) e^{-1} \right]$$

6) Generalized Exponential on a Pedestal ( $\alpha$  is arbitrary)

$$\varepsilon_r(\rho) = \left( \frac{\varepsilon_r(0) - 1}{1 - e^{-\alpha}} \right) e^{-\alpha(\rho/R)} + \left[ 1 - \left( \frac{\varepsilon_r(0) - 1}{1 - e^{-\alpha}} \right) e^{-\alpha} \right]$$

7) Cosine on a Pedestal (flat at  $\rho = 0$  and  $\rho = R$ )

$$\varepsilon_r(\rho) = \left( \frac{\varepsilon_r(0) - 1}{2} \right) \cos\left(\frac{\pi\rho}{R}\right) + \left[ \frac{\varepsilon_r(0) + 1}{2} \right]$$

8) Gaussian on a Pedestal

$$\varepsilon_r(\rho) = \left( \frac{\varepsilon_r(0) - 1}{1 - e^{-1}} \right) e^{-(\rho/R)^2} + \left[ 1 - \left( \frac{\varepsilon_r(0) - 1}{1 - e^{-1}} \right) e^{-1} \right]$$

9) Generalized Gaussian on a Pedestal ( $\alpha$  is arbitrary)

$$\varepsilon_r(\rho) = \left( \frac{\varepsilon_r(0) - 1}{1 - e^{-\alpha}} \right) e^{-\alpha(\rho/R)^2} + \left[ 1 - \left( \frac{\varepsilon_r(0) - 1}{1 - e^{-\alpha}} \right) e^{-\alpha} \right]$$

10) Generalized Hyper-Gaussian on a Pedestal ( $\alpha$  and  $n$  are arbitrary)

$$\varepsilon_r(\rho) = \left( \frac{\varepsilon_r(0) - 1}{1 - e^{-\alpha}} \right) e^{-\alpha(\rho/R)^n} + \left[ 1 - \left( \frac{\varepsilon_r(0) - 1}{1 - e^{-\alpha}} \right) e^{-\alpha} \right]$$

11) Tanh with breakpoint in the middle ( $\alpha$  is arbitrary)

$$\varepsilon_r(\rho) = - \left( \frac{\varepsilon_r(0) - 1}{2 \operatorname{Tanh}(\alpha/2)} \right) \operatorname{Tanh}\left(\alpha \frac{(\rho - R/2)}{R}\right) + \left[ 1 + \left( \frac{\varepsilon_r(0) - 1}{2 \operatorname{Tanh}(\alpha/2)} \right) \operatorname{Tanh}\left(\frac{\alpha}{2}\right) \right]$$

12) Tanh with arbitrary breakpoint ( $\alpha$  and  $b$  are arbitrary, with  $0 < b < R$ )

$$\varepsilon_r(\rho) = - \left[ \frac{\varepsilon_r(0) - 1}{\left( \text{Tanh}\left(\alpha \frac{b}{R}\right) + \text{Tanh}\left(\frac{R-b}{R}\right) \right)} \text{Tanh}\left(\alpha \frac{(\rho-b)}{R}\right) \right. \\ \left. + 1 + \left[ \frac{\varepsilon_r(0) - 1}{\left( \text{Tanh}\left(\alpha \frac{b}{R}\right) + \text{Tanh}\left(\frac{R-b}{R}\right) \right)} \text{Tanh}\left(\frac{R-b}{R}\right) \right] \right]$$

13) Tanh with Quadratic Argument ( $\alpha$  is arbitrary)

$$\varepsilon_r(\rho) = \varepsilon_r(0) - \left( \frac{\varepsilon_r(0) - 1}{\text{Tanh}(\alpha)} \right) \text{Tanh}\left(\alpha (\rho/R)^2\right)$$

14) Exponential with Quadratic ( $\alpha$  is arbitrary)

$$\varepsilon_r(\rho) = \varepsilon_r(0) - \left( \frac{\rho}{R} \right)^2 \left( \frac{\varepsilon_r(0) - 1}{e^{-\alpha}} \right) e^{-\alpha(\rho/R)^2}$$

## B. Matlab and Mathcad Programs for Analytical Solution

```
clear all;
clear functions;
clear functionname;
clear plots;
close all;
base_dielectric=1.4030
Percent_tapered=.97
b=base_dielectric
p=percent_tapered
number=22 %based on 22 rings currently
R=.248 %Radius of structure
inputhinmm=92 %height in mm
h1=inputhinmm/10^3;
ER=[b*p b*p^2 b*p^3 b*p^4 b*p^5 b*p^6 b*p^7 b*p^8 b*p^9 b*p^10 b*p^11
b*p^12 b*p^13 b*p^14 b*p^15 b*p^16 b*p^17 b*p^18 b*p^19 b*p^20 b*p^21
1]
KZNF=[0 0 0 0 0 0 0 0 0 0 0 0 0 0 0 0 0 0 0 0 0];
coeff=[0 0 0 0];
k=number+1;
n=1;
while (k>n);

kznl=2.13;
kzn=.9;
while kznl>kzn;
    er1=ER(n);
    uo=4*3.14*10^-7;
    c=2.99792458*10^8;
    eo=1/(c^2*uo);
    f=2.0*10^9;
    w=2*3.14*f;
    ko=w*sqrt(uo*eo);
    kyoin=sqrt(ko^2-(kzn*ko)^2);
    er2=1;
    h2=.00000001;
    er3=1;
    h3=.00000001;

a=(imag(kyoin));
if a==0 ;
    b=0;
else a=a;
end;
    if a>0;

    b=1;
    else;
    b=-1;
    end;
kyo=-kyoin*b;

    k1=ko*sqrt(er1);
    k2=ko*sqrt(er2);
```

```

        k3=ko*sqrt(er3);
        ky1=sqrt(k1^2-(kzn*ko)^2);
        ky2=sqrt(k2^2-(kzn*ko)^2);
        ky3=sqrt(k3^2-(kzn*ko)^2);
Z1=ky1/(w*eo*er1);
Z2=ky2/(w*eo*er2);
Z3=ky3/(w*eo*er3);
Zin1=j*Z1*tan(h1*ky1);
Zin2=Z2*(Zin1+j*Z2*tan(h2*ky2))/(Z2+j*Zin1*tan(h2*ky2));
Zin3=Z3*(Zin2+j*Z3*tan(h3*ky3))/(Z3+j*Zin2*tan(h3*ky3));
Zin=Zin3;
Zo=kyo/(w*eo);
TRE=Zin+Zo;
TREA=abs(TRE);
if (TREA<.1); %convergence error allowed to find Beta
    KZNF(n)=kzn*ko;
    kzn=4;
else
end
kzn=kzn+.000005; %steps required to get most answers. Need to avoid a 0
answer
end

n=n+1;

end
ERR = fliplr(ER);
Beta=KZNF./ko
%plot(ERR,KZNF,'red')
xlabel('Ring from inner to outer');
ylabel('Beta');
%hold on
%curve fit polynomial form
a=6.5954e-004:.4887/10+.0487/10:0.4887
b=KZNF./40 %if you want normalized Beta
c=sum(b)./22 %average Beta
%coeff = polyfit(a,b,4) %fourth order polynomial
coeff3 = polyfit(a,b,2) %second order polynomial
%curve=coeff(1).*a.^4+coeff(2).*a.^3+coeff(3).*a.^2+coeff(4).*a+coeff(5)
)
curve2=coeff3(1).*a.^2+coeff3(2).*a.^1+coeff3(3)
%plot (a, curve2)
%hold on
%plot(a,curve2)
syms X
%curve=coeff(1).*X.^4+coeff(2).*X.^3+coeff(3).*X.^2+coeff(4).*X+coeff(5)
);
curveF=coeff3(1).*X.^2+coeff3(2).*X.^1+coeff3(3)
Beta_function=vpa(curveF);
Beta=int(curveF,X,0,X)
Integral=vpa(Beta)

```

INPUT PARAMETERS

$$R := RN \cdot \lambda_0$$

$$f := 2.0 \cdot 10^9$$

$$\beta N_{ini} := 1.243$$

$$RN := 3.27$$

$$\beta_{HW} := k_0 + \frac{2.94}{R}$$

$$\beta(t) := k_0 \left[ \beta N_{ini} - \left( \frac{\beta N_{ini} - 1.0}{R} \right) \cdot t \right]$$

$$\frac{\beta_{HW}}{k_0} = 1.14309$$

FUNDAMENTAL CONSTANTS

$$I(\rho) := \int_0^{\rho} \beta(t) dt$$

$$\beta_{Nave} := \frac{\beta N_{ini} + 1}{2}$$

$$c := 2.99792458 \cdot 10^8$$

$$F(\theta) := \int_0^R H_2(0, I(\rho)) \cdot J_1(k_0 \rho \cdot \sin(\theta)) \cdot \rho d\rho$$

$$\beta_{Nave} = 1.1215$$

$$\mu_0 := 4 \cdot \pi \cdot 10^{-7}$$

$$G(\theta \text{ deg}) := \left| \frac{F\left(\theta \text{ deg} \cdot \frac{\pi}{180}\right)}{F\left(\frac{\pi}{2}\right)} \right|$$

$$\epsilon_0 := \frac{1}{c^2 \cdot \mu_0}$$

$$\eta_0 := \sqrt{\frac{\mu_0}{\epsilon_0}}$$

$$F_{function} := \int_0^{\frac{\pi}{2}} \left( \left| \frac{F(\theta)}{F\left(\frac{\pi}{2}\right)} \right| \right)^2 \cdot \sin(\theta) d\theta$$

$$\lambda_0 := \frac{c}{f}$$

$$k_0 := \frac{2 \cdot \pi}{\lambda_0}$$

$$D_{norm} := \frac{1}{F_{function}}$$

**c. HFSS Model Specification based on Modified HW Condition**

<b>Ring Number</b>	<b>Dielectric Constant</b>	
	<b>1% Taper</b>	<b>.1% Taper</b>
1	1.403	1.402
2	1.389	1.401
3	1.375	1.399
4	1.361	1.398
5	1.348	1.396
6	1.334	1.395
7	1.321	1.394
8	1.308	1.392
9	1.295	1.391
10	1.282	1.389
11	1.269	1.388
12	1.256	1.387
13	1.244	1.385
14	1.231	1.384
15	1.219	1.382
16	1.207	1.381
17	1.195	1.380
18	1.183	1.378
19	1.171	1.377
20	1.159	1.376
21	1.148	1.374
22	1.136	1.373

#### D. Summary of DSWA Design Specifications

Tapers	Structure Length [ $\lambda_o$ ]	Beamwidth [deg]	Side lobe level [dB]	Directivity [dB]	Height [mm]	Probe Height [mm]	$\beta_{AVG}$	$\beta_{HW}$
<b>6% Taper w/base <math>\epsilon_r</math> 4.6</b>	3.27	17.0	-13.10	8.19	14.8	14	1.0885	1.143
<b>5% Taper w/base <math>\epsilon_r</math> 4.6</b>	3.27	15.0	-12.90	8.37	14.8	14	1.1030	1.143
<b>4% Taper w/base <math>\epsilon_r</math> 4.6</b>	3.27	14.0	-10.90	8.39	14.8	14	1.1200	1.143
<b>3% Taper w/base <math>\epsilon_r</math> 3.7</b>	3.27	14.0	-10.36	8.40	15.6	15	1.1261	1.143
<b>2% Taper w/ base <math>\epsilon_r</math> 3.7</b>	3.27	13.5	-10.67	8.41	15.6	15	1.1261	1.143
<b>1% Taper w/base <math>\epsilon_r</math> 1.47</b>	3.27	11.5	-10.46	9.40	92.0	65	1.1126	1.143
<b>1% Taper w/base <math>\epsilon_r</math> 1.403</b>	3.27	12.5	-17.05	9.60	121.0	71	1.0860	1.143
<b>.1% Taper w/base <math>\epsilon_r</math> 1.402</b>	3.27	10.0	-13.12	11.06	121.0	71	1.0115	1.143
<b>.1% Taper w/base <math>\epsilon_r</math> 1.402</b>	4.46	8.50	-11.17	12.19	137.5	71	1.0115	1.105
<b>.1% Taper w/base <math>\epsilon_r</math> 1.402</b>	4.46	7.50	-10.68	14.37	150.0	71	1.0115	1.105
<b>.1% Taper w/base <math>\epsilon_r</math> 1.3</b>	6.00	6.00	-13.01	16.21	150.0	71	1.0256	1.078
<b>Linear (1.99-1)</b>	0.41	15.5	-10.33	2.81	125.0	71	1.061	2.14
<b>Linear(1.9-1)</b>	0.82	14.3	-10.33	6.47	125.0	71	1.077	1.57
<b>Linear(1.89-1)</b>	1.09	13.0	-11.97	9.15	125.0	71	1.07	1.43
<b>Linear(1.85-1)</b>	1.64	10.5	-10.32	10.87	125.0	71	1.061	1.29
<b>Linear(1.7-1)</b>	3.27	8.5	-10.01	11.04	162.5	71	1.0674	1.14
<b>Linear(1.5-1)</b>	6.54	5.5	-11.83	15.81	200.0	71	1.0546	1.10
<b>Linear(1.35-1)</b>	11	4.5	-12.35	19.1	240	71	1.0362	1.04

